



















RESEARCH ARTICLE | JULY 24 2025

Validation of a comprehensive first-principles-based framework for predicting the performance of future stellarators ^{EP}

Special Collection: [Papers from the 66th Annual Meeting of the APS Division of Plasma Physics](#)

D. L. C. Agapito Fernando ; A. Bañón Navarro ; D. Carralero ; A. Alonso ; A. Di Siena ; J. L. Velasco ; F. Wilms ; G. Merlo ; F. Jenko ; S. A. Bozhnikov ; E. Pasch; G. Fuchert ; K. J. Brunner ; J. Knauer ; A. Langenberg ; N. A. Pablant ; T. Gonda ; O. P. Ford ; L. Vanó ; T. Windisch ; T. Estrada ; E. Maragkoudakis ; the Wendelstein 7-X Team



Phys. Plasmas 32, 073904 (2025)

<https://doi.org/10.1063/5.0267879>



Articles You May Be Interested In

Assessing core ion thermal confinement in critical-gradient-optimized stellarators

Phys. Plasmas (June 2024)

Theoretical interpretation of W soft X-ray spectra collected by the pulse height analysis system on Wendelstein 7-X stellarator

Phys. Plasmas (June 2024)

Bounce-averaged drifts: Equivalent definitions, numerical implementations, and example cases

Phys. Plasmas (September 2023)

01 August 2025 07:56:00



Physics of Plasmas

Special Topics Open
for Submissions

[Learn More](#)

Validation of a comprehensive first-principles-based framework for predicting the performance of future stellarators

Cite as: Phys. Plasmas **32**, 073904 (2025); doi: [10.1063/5.0267879](https://doi.org/10.1063/5.0267879)

Submitted: 26 February 2025 · Accepted: 23 June 2025 ·

Published Online: 24 July 2025



View Online



Export Citation



CrossMark

D. L. C. Agapito Fernando,^{1,a)} A. Bañón Navarro,¹ D. Carralero,² A. Alonso,² A. Di Siena,¹ J. L. Velasco,² F. Wilms,¹ G. Merlo,¹ F. Jenko,^{1,3} S. A. Bozhnikov,⁴ E. Pasch,⁴ G. Fuchert,⁴ K. J. Brunner,⁴ J. Knauer,⁴ A. Langenberg,⁴ N. A. Pablant,⁵ T. Gonda,⁶ O. P. Ford,⁴ L. Vanó,⁴ T. Windisch,⁴ T. Estrada,² E. Maragkoudakis,² and the Wendelstein 7-X Team^{b)}

AFFILIATIONS

¹Max-Planck-Institut für Plasmaphysik, Boltzmannstraße 2, 85748 Garching bei München, Germany

²Laboratorio Nacional de Fusion, CIEMAT, 28040 Madrid, Spain

³Institute for Fusion Studies, The University of Texas at Austin, Austin, Texas 78712, USA

⁴Max-Planck-Institut für Plasmaphysik, Wendelsteinstraße 1, 17491 Greifswald, Germany

⁵Princeton Plasma Physics Laboratory, 100 Stellarator Road, Princeton, New Jersey 08543, USA

⁶Auburn University Physics Department, 380 Duncan Dr., Auburn, Alabama 36832, USA

Note: This paper is part of the Special Collection: Papers from the 66th Annual Meeting of the APS Division of Plasma Physics.

Note: Paper N12 5, Bull. Am. Phys. Soc. **69** (2024).

^{a)}Invited speaker. **Author to whom correspondence should be addressed:** don.fernando@ipp.mpg.de

^{b)}For the complete member list, please refer to O. Grulke et al., Nucl. Fusion **64**, 112002 (2024).

ABSTRACT

This paper presents the validation of the GENE-KNOSOS-Tango framework for recovering both the steady-state plasma profiles in the considered radial domain and selected turbulence trends in a stellarator. This framework couples the gyrokinetic turbulence code GENE, the neo-classical transport code KNOSOS, and the transport solver Tango in a multi-timescale simulation feedback loop. Ion-scale kinetic-electron and electron-scale adiabatic-ion flux-tube simulations were performed to evolve the density and temperature profiles for four OP1.2b W7-X scenarios. The simulated density and temperature profiles showed good agreement with the experimental data using a reasonable set of boundary conditions. Equally important was the reproduction of observed trends for several turbulence properties, such as density fluctuations and turbulent heat diffusivities. Key effects were also touched upon, such as electron-scale turbulence and the neoclassical radial electric field shear. The validation of the GENE-KNOSOS-Tango framework enables credible predictions of physical phenomena in stellarators and reactor performance based on a given set of edge parameters.

© 2025 Author(s). All article content, except where otherwise noted, is licensed under a Creative Commons Attribution (CC BY) license (<https://creativecommons.org/licenses/by/4.0/>). <https://doi.org/10.1063/5.0267879>

I. INTRODUCTION

Within the field of nuclear fusion by magnetic confinement, stellarators are a promising alternative to tokamaks, offering several notable advantages. To name a few, stellarators are inherently capable of operating at steady-state, have higher plasma density limits, exhibit lower peak heat flux exhaust, and avoid major disruptions.¹ With improved optimization for magnetohydrodynamic (MHD) stability and neoclassical transport, turbulence remains a significant obstacle for stellarators today. For instance, turbulence-driven transport

surpasses the neoclassical contribution in Wendelstein 7-X (W7-X), the most advanced stellarator to date.² Thus, understanding plasma turbulence is crucial for designing stellarators and advancing fusion reactor development.

With the world's most powerful supercomputers, turbulence can now be analyzed across the entire plasma volume using gyrokinetic codes. Although gyrokinetic codes are capable of simulating the effect of turbulence on plasma temperature and density profiles up to energy confinement times, this task demands an extremely large amount of

computational resources. The challenge stems from the large timescale separation between turbulence and transport phenomena. Despite this, profile prediction remains a key research goal in fusion. Developing simulation tools capable of doing so for a given magnetic configuration using only the power and particle sources is essential for designing operational scenarios with optimized confinement and turbulence properties and forecasting reactor performance.

An effective strategy for bridging the timescale gap is to couple a gyrokinetic code and a transport solver in a feedback loop. Instead of being hindered by the timescale gap, this coupling exploits it, leading to a significant reduction in the computational cost of simulating steady-state plasma profiles. The turbulence code computes the turbulent fluxes for input plasma profiles using gradient-driven simulations, while the transport solver evolves the profiles according to the difference between the fluxes and sources. This approach has been successfully applied and validated for tokamaks using both flux-tube^{3–6} and global^{7,8} gyrokinetic simulations.

To extend this capability for stellarators, we further developed the existing GENE-Tango suite^{7,8} to create the GENE-KNOSOS-Tango framework. This framework couples the gyrokinetic turbulence code GENE,⁹ the neoclassical transport code KNOSOS,^{10,11} and the one-dimensional transport solver Tango^{7,12,13} in a multiple-timescale simulation feedback loop. It self-consistently incorporates turbulence, neoclassical transport, and the neoclassical radial electric field shear in each iteration. The framework can be extended to include three-dimensional effects by using GENE-3D.^{14,15}

The GENE-KNOSOS-Tango framework has previously been used to study the confinement degradation in electron-heated W7-X plasmas, as evidenced by the ion-temperature clamping, during the machine's first experimental campaign.^{16–18} Additionally, it has been used to compare the core confinement properties of the HSX (Helically Symmetric Experiment) stellarator and the HSK (Helically Symmetric Kompakt stellarator) and QSTK (Quasi-Symmetric Turbulence Konzept), two quasi-helically symmetric stellarator configurations optimized for ion temperature gradient (ITG) stability.¹⁹

Although it has already been successfully applied to stellarator studies, the framework's validation remains necessary to ensure that simulation predictions reproduce experimental results and turbulence features across a wide range of operating conditions. Accurately recovering plasma profiles and key trends is essential in such validation studies. Validation efforts are a prerequisite for enabling profile predictions, developing operation scenarios, and designing future reactors. The latter is of utmost importance in the current context, where the increasing number of nuclear fusion startups is leveraging simulation codes to design power-generating machines for the near future. To date, the only other coupled code validation study for the core that is being performed for stellarators is for the gyrokinetic code GX,^{20,21} transport code Trinity3D,^{4,22} and neoclassical codes KNOSOS and SFINCS.^{23–25}

In this study, we present the validation of the GENE-KNOSOS-Tango framework using four scenarios from the OP1.2b W7-X experimental campaign.^{17,26} These cases cover a wide range of turbulence properties, effectively adding another constraint to the validation task. In addition to matching the targeted experimental results for each scenario, the framework should also model selected trends among different turbulence regimes. This ensures the robustness and applicability of the framework across diverse experimental conditions. Improvements on previous work include the addition of kinetic-electron

gyrokinetic simulations in each iteration, neoclassical effects, and varying density profiles.

This paper is structured as follows: An overview of the four experimental cases is presented in Sec. II. Next, in Sec. III, a more in-depth description on the GENE-KNOSOS-Tango framework is provided. In Sec. IV, the simulation setup and methodology are discussed. The simulation results are presented in Sec. V. Finally, a summary of the findings, conclusion, and outlook is given in Sec. VI.

II. W7-X SCENARIOS

Three W7-X discharges from OP1.2b were used for this study, and these give way to four different scenarios. Figure 1 shows the time traces for the heating power, average densities, and stored energies of these discharges. The naming convention for the four scenarios used in Refs. 17 and 26 will be retained in this paper for consistency. The first two scenarios are characterized by a core ion temperature T_i below 1.5 ± 0.2 keV, which is typical of W7-X electron-heated plasmas,¹⁶ while the last two exceed this threshold value. For these scenarios, the ion species is hydrogen.

The first two cases are shots 180 920.013 and 180 920.017, which were purely heated by electron cyclotron resonance (ECRH) and fueled with gas puffing. Case 1 is the “low-density ECRH” scenario while case 2 is the “high-density ECRH” case, which have average densities of about 4 and $6 \times 10^{19} \text{ m}^{-3}$ respectively. The same heating power of about 4.7 MW was applied to both.

From shot 180 919.039, two neutral-beam injection (NBI) heating cases are derived based on different timestamps during the shot. Case 3, which is the “NBI + ECRH” scenario, was taken at a timestamp of about 3.5 s and had a higher ECRH power than case 4, the “NBI” scenario, which was taken at 4.5 s. It should be emphasized that even though case 4 is referred to as the “NBI” scenario, about 0.7 MW of ECRH was still present. The total heating power for case 3 was approximately 8 MW, while case 4 only received about 4 MW due to the significant reduction of applied ECRH power.

III. FRAMEWORK DESCRIPTION

To predict the core temperature and density profiles for these scenarios, the state-of-the-art GENE-KNOSOS-Tango framework is used. The gyrokinetic turbulence code GENE simulates the turbulent transport of each plasma species, while the neoclassical transport code KNOSOS calculates the neoclassical fluxes and the background neoclassical radial electric field E_r . Then, the transport solver Tango performs several tasks, such as calculating the neoclassical $E_r \times B$ shear, which is fed back to GENE, and calculating a particle source component using mathematical models.

Most importantly, Tango generates the new plasma profiles by comparing the total fluxes with the injected sources. The code accomplishes this by solving one-dimensional radial transport equations for pressure and density. The flux is assumed to have a convective and diffusive part, which rely on the profiles and their gradients, respectively,

$$Q = -D_Q \frac{\partial p}{\partial \rho} + c_Q p, \quad (1)$$

$$\Gamma = -D_\Gamma \frac{\partial n}{\partial \rho} + c_\Gamma n. \quad (2)$$

In the above equations, ρ denotes the radial coordinate, Q is the heat flux, Γ is the particle flux, p is the pressure, and n is the density, while

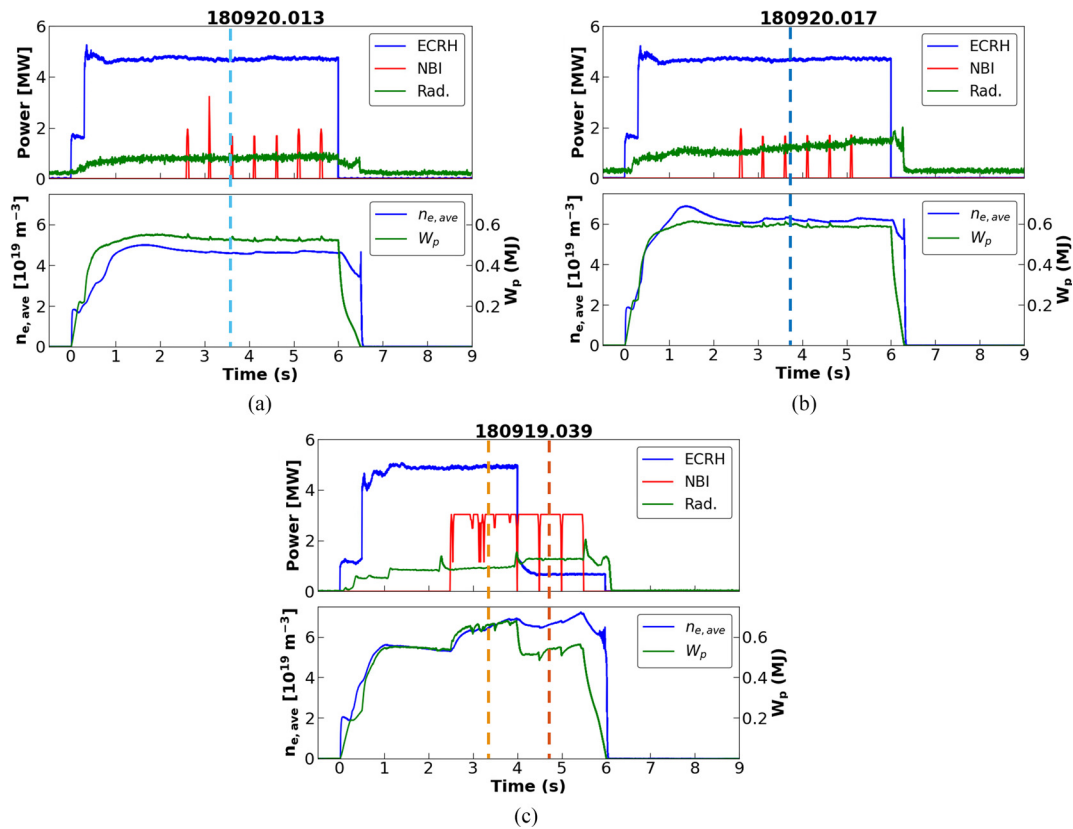


FIG. 1. The three OP1.2b W7-X discharges used for this validation study: (a) low-density with ECRH, (b) high-density with ECRH, and (c) NBI with different ECRH power. Upper plots show the time traces for the input and radiated power, while the lower plots show the average densities and stored energies. Dashed lines indicate the timestamps when the experimental data were obtained for each scenario.¹⁷

D and c are the diffusive and convective transport coefficients, respectively. It should be noted that the momentum transport equation is not yet implemented in Tango but will be added soon to extend the framework's applicability to a broader set of magnetic geometries. While momentum evolution can influence the converged plasma profiles, its impact is expected to be minor in non-quasisymmetric stellarators like W7-X, where rotation is much slower than the ion thermal speed.²⁷ A relaxation scheme is applied to the fluxes and profiles, wherein iterated values from two successive iterations are linearly combined. The magnitude of the weighting parameter w determines the level of relaxation. Turbulent transport exhibits stiff behavior physically, in that it rapidly grows beyond a threshold gradient value,²⁸ and numerically, since the diffusive transport coefficient's strong dependence on the profile's radial gradient renders the numerical method unstable.^{12,29} Due to these factors, small changes in plasma gradients can lead to large changes in transport level. Tango's relaxation parameter dampens these large swings and prevents excessive oscillations of the fluxes around the source values, thereby keeping the numerical method well-behaved. Typically, w values of 0.1–0.3 are used. Moreover, relaxation reduces the statistical variance of the turbulence simulations as a result of averaging over consecutive iterations.¹³

The new profiles are read by GENE and KNOSOS in the next iteration, and the feedback loop continues as needed. Convergence is

manually determined based on the fulfilment of the radial power and particle balances. The full framework showing the coupling and dependencies between the codes is depicted in Fig. 3(c).

A demonstration of how the GENE-KNOSOS-Tango framework evolves the plasma profiles is shown in Fig. 2. As a rule of thumb, fluxes that overshoot the sources at a given position will result in a local flattening of the relevant profile, while the profile is steepened at positions where the fluxes are under-predicted. In Fig. 2, approximately flat profiles were used as initial guesses for plasma temperatures and density. In the context of the profiles, only the boundary values are absolutely important for Tango; the code will adjust every other point in the profile to satisfy the power and particle balances without the need for any external user prompt. However, while convergence can still be achieved, using poorly chosen initial profile guesses typically requires more iterations before balances are satisfactorily fulfilled. In this case, about 50 iterations were needed. Persistent discrepancies in the power and particle balances arise from the limited number of flux tubes used in the simulations. Increasing the number of radial positions improves the agreement by allowing Tango more flexibility to adjust the profile gradients, but at the cost of higher computational effort due to performing more GENE simulations per iteration.

To make the validation study possible, the capabilities of Tango were expanded through the addition of a neoclassical $E_r \times B$ shear

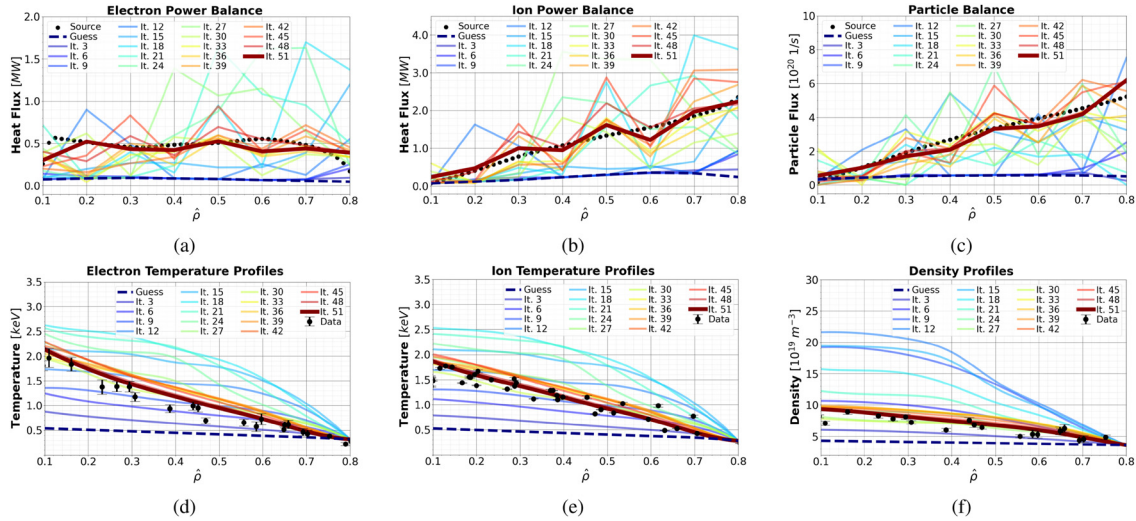


FIG. 2. Demonstration of how the GENE-KNOSOS-Tango framework evolves the (d) electron temperature, (e) ion temperature, and (f) density profiles, which were all given initial guesses that are approximately flat. Convergence of the (a) electron power, (b) ion power, and (c) particle balances was achieved in about 50 iterations.

calculation scheme³⁰ and a particle source model based on neutrals ionization. For the former, the radial derivative of the $E_r \times B$ velocity is linearized and evaluated at each radial position of interest. The shear rate γ_E modifies the coordinate system of the simulation domain, specifically the radial dimension as well as radial derivatives, in the co-moving frame. Reference 31 outlines how this is implemented in GENE. In Eq. (3), normalized dimensionless quantities are used, as signified by the circumflex accent. The magnetic shear is given by \hat{s} .

$$\hat{\gamma}_E(\hat{\rho}_0) = -\frac{d}{d\hat{\rho}} \left(\frac{\hat{E}_r(\hat{\rho})}{\hat{B}(\hat{\rho})} \right) \bigg|_{\hat{\rho}=\hat{\rho}_0} = -\left[\frac{d\hat{E}_r}{d\hat{\rho}} - \frac{\hat{E}_r}{\hat{\rho}}(1-\hat{s}) \right] \bigg|_{\hat{\rho}=\hat{\rho}_0}. \quad (3)$$

For the latter, the neutral density radial profile, $n_0(\hat{\rho})$, is calculated using a short-mean-free-path one-dimensional transport model^{32,33}

$$\frac{1}{\rho} \frac{d}{d\rho} \left[\rho \left(\frac{T_0}{m_0 \nu_{CX}} \right) \left(\frac{dn_0}{d\rho} + \frac{1}{T_0} \frac{dT_0}{d\rho} n_0 \right) \right] = \nu_{ion} n_0. \quad (4)$$

In Eq. (4), T_0 and m_0 are the neutral species temperature and mass, respectively. The ionization and charge exchange frequencies are given by ν_{ion} and ν_{CX} , respectively. These are calculated by evaluating the analytical fits of the ionization and charge exchange cross sections of hydrogen at the plasma parameters.^{34,35} That being said, it is assumed in the model that plasma ions and neutrals have the same temperature profile due to the high frequency of collisions and charge exchange reactions occurring between them. It is important to point out that the neutrals density at the outer boundary, $n_{0,edge}$, is a free parameter in Eq. (4). Reported measurements in W7-X electron-cyclotron-heated plasmas^{16,36} and particle confinement time calculations³⁷ were used as bases for $n_{0,edge}$ input values in Tango.

The ionization rate of neutral species provides a particle source term for the density transport equation. In addition to this, for cases 3 and 4, the NBI particle fueling rates were obtained from BEAMS3D^{38–40}

simulations. Two fueling rates are provided by BEAMS3D, one for the electrons and another one for the thermal ions. The latter is slightly smaller than the former due to fast ion losses. Due to uncertainties with the degree of thermalization of the NBI ions, the electron fueling rate is used as the particle source for both plasma electrons and ions. This greatly simplified the simulations for this study; dedicated three-species simulations will be explored in a future study. On the other hand, for the pressure equation, heat sources and sinks consist of the ECRH and NBI power deposition profiles calculated using TRAVIS⁴¹ and BEAMS3D, respectively, and the collisional thermalization⁴² between ions and electrons calculated in Tango.

IV. SIMULATION SETUP AND MODEL HIERARCHY

Instead of applying the full framework immediately, a model hierarchy was adapted in which physics is incrementally added to the simulations. This way, it is easier to understand how each of these effects can impact the converged plasma state. Furthermore, the selection of the four phases was also based on increasing simulation complexity. The workflow has four phases, as seen in Fig. 3, and the converged plasma profiles of one phase are used as initial inputs for the next one. The choice and ordering of these phases does not impact the final result; a different workflow could have been adopted, and the same converged profiles would have been obtained in the end.

For phase 1, only GENE and Tango were included in the simulation loop, and the density profiles were kept fixed. As such, only the temperature profiles were varied based on how well the power balances had been met. To decrease the number of iterations necessary to reach convergence, the statistical fits of the experimental profiles were used as the initial guesses for the plasma profiles. Dirichlet boundary conditions are applied to the outermost radial position, where the temperature and density values are fixed. In contrast, Neumann boundary conditions are used at the innermost position, giving way to plasma profiles with zero radial gradient on the magnetic axis.^{7,13} The converged phase 1 plasma profiles were used as initial guesses for phase 2, where neoclassical heat fluxes were computed by KNOSOS. The

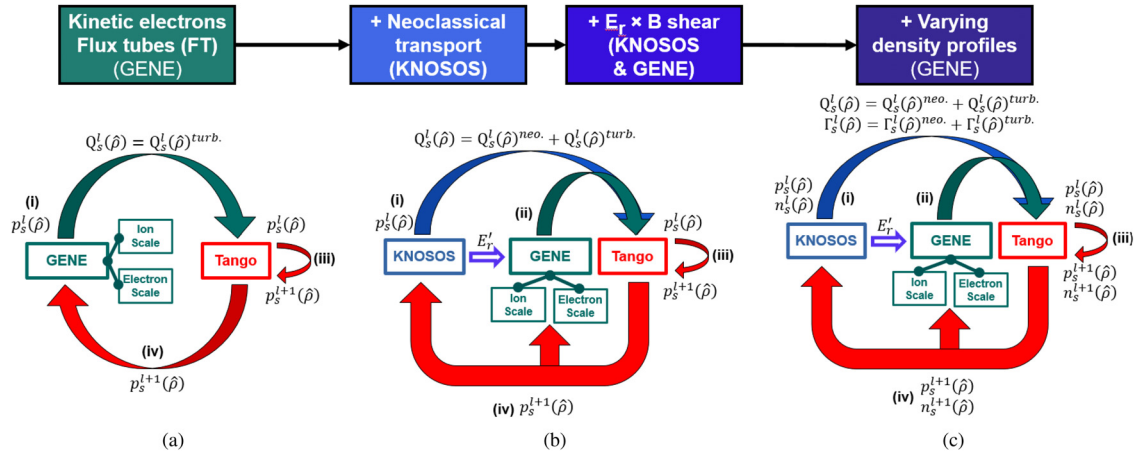


FIG. 3. Model hierarchy of the GENE-KNOSOS-Tango framework: (a) Fixed-density simulations without neoclassical transport, (b) inclusion of KNOSOS in the loop for calculating neoclassical heat fluxes, calculation of the neoclassical $E_r \times B$ shear for GENE simulations, and (c) full framework with varying density profiles. The superscript l denotes the iteration number while $neo.$ and $turb.$ pertain to the neoclassical and turbulent flux contributions, respectively. The subscript s represents the species. The variable p denotes the plasma pressure, while n is the density. Finally, the heat and particle fluxes are Q and Γ , respectively.

neoclassical radial electric field E_r from KNOSOS was passed to Tango in phase 3 to determine the neoclassical $E_r \times B$ shear profile. This was used as an additional input to GENE. Finally, in phase 4, the constraint on keeping the density profile fixed was lifted. With this, the particle fluxes, both turbulent from GENE and neoclassical from KNOSOS, were taken into account by Tango, which now also solved the transport equation for density.

For the GENE simulations, eight radial positions spanning $\hat{\rho}$ of 0.1–0.8 with a spacing of 0.1 were selected. The dimensionless radial coordinate $\hat{\rho} = \sqrt{\Psi/\Psi_{LCFS}}$ is defined by the magnetic toroidal flux passing through a given magnetic surface, Ψ , and the last closed flux surface (LCFS). At each $\hat{\rho}$ and each iteration, ion-scale kinetic-electron and electron-scale adiabatic-ion flux-tube simulations were performed using the flux tube with the field line label $\alpha = 0$. The simulations are all electromagnetic, although the heat and particle fluxes are mostly electrostatic due to the low β of the explored scenarios.

The choice for this radial domain of the simulations was motivated by the task of validating the framework over a large portion of the stellarator core while keeping the computational costs of the study tractable. First, adding an additional point close to the magnetic axis ($\hat{\rho} \approx 0.0$) was deemed unnecessary since the heat and particle fluxes in this region are generally negligible. While on-axis heating can be significant in some cases, its impact is tempered by the small plasma volume near the axis. Moreover, the quantities in this region are not measured well experimentally, providing less motivation to compare simulated results for $\hat{\rho} < 0.1$ with experimental data. Next, there were some considerations for limiting the simulations to $\hat{\rho} = 0.8$. Simulations in the vicinity of the LCFS at $\hat{\rho} = 1.0$ will require a higher resolution in at least the radial and parallel directions due to the larger magnetic shear and stronger plasma shaping close to the plasma edge, respectively. More importantly, the kinetic simulations are only two-species with hydrogen ions and electrons forming the plasma. As one moves closer to the LCFS, the effects of impurities and neutrals on the turbulence become increasingly important. In this case, they could have a large effect on the plasma and should no longer be disregarded.

For instance, high impurity concentrations lead to higher radiation losses, which will subsequently reduce plasma temperatures.

Before starting any of the phases, convergence tests were first performed to determine the nominal resolution parameters that would be used throughout the study. After convergence had been achieved with respect to both power and particle balances in phase 4, several high-resolution runs were carried out to ensure that heat and particle fluxes stayed within $\pm 20\%$ of the values obtained using the nominal resolution. This allowance is justified by the stiffness of the fluxes, as a moderate change in fluxes only slightly alters the gradients and, consequently, the profiles. Table I shows the numerical parameters for nominal and high resolution, where l_i and n_i are the extension of the simulation box and the number of grid points in the i dimension, respectively. The minimum value of the binormal wavenumber is given by k_{ymin} . The resolution parameters in the y -direction for the electron-scale simulation remain unchanged between the nominal-

TABLE I. Numerical parameters for the resolution of the GENE simulations. The parameters l_x , $l_{y\parallel}$, and l_μ are given in units of ρ_s , $v_{T,s} = \sqrt{2T_s/m_s}$, and T_s/B_{ref} , respectively.

Parameter	Ion scale		Electron scale	
	Nominal	High	Nominal	High
l_x	128	256	128	256
n_{k_x}	64	256	64	256
k_{ymin}	0.10	0.05	0.075	0.075
n_{k_y}	32	64	48	48
n_z	96	128	96	128
$l_{y\parallel}$	2.5	3	2.5	3
$n_{y\parallel}$	16	48	16	48
l_μ	9	9	9	9
n_μ	12	12	12	12

and high-resolution cases since these were constrained by the separation of ion- and electron-scales. Equation (5) must hold true to ensure that no overlap between the k_y ranges of the two simulations occurred

$$k_{y_{min,e}} \rho_e = \sqrt{\frac{m_i}{m_e}} k_{y_{min,e}} \rho_i > k_{y_{max,i}} \rho_i. \quad (5)$$

In this equation, ρ_s is the reference gyroradius for species s . It is given by the following equation, where T_{ref} is the reference temperature, m is the mass, q is the charge, and B_{ref} is the reference magnetic field strength obtained from the geometry file input to GENE:

$$\rho_s = \frac{c_s}{\Omega_s} = \sqrt{\frac{T_{ref}}{m_s}} \left(\frac{q_s B_{ref}}{m_s} \right)^{-1}. \quad (6)$$

Moreover, sufficient numerical hyperdiffusion was applied to the higher wavenumbers of the ion-scale simulation so that its flux spectra smoothly goes to zero toward the end of the k_y range. This prevents any pileup in the fluxes due to the intermediate- and electron-scales. A sample electrostatic heat flux spectrum for the electrons is shown in Fig. 4.

Since $k_{y_{min}}$ was not modified, n_{k_y} was maintained at the nominal value as well so that the high-resolution simulation covers the same k_y range. Finally, it should be noted that the actual value of radial box extent in units of gyroradii, l_x , used by GENE is not always equal to the input due to its quantization based on $k_{y_{min}}$, the magnetic shear \hat{s} , the safety factor q , and other parameters. In practice, l_x became as low as 80 in some cases, giving a radial resolution close to one gyroradius. However l_x was always equal to 128 for $\hat{\rho} \leq 0.4$ in nominal-resolution runs since \hat{s} was forcibly set to zero. This lifted the quantization restriction on l_x , allowing us to use the relatively low numerical resolution in the radial direction. As a result, the periodic parallel boundary condition was applied for $\hat{\rho} \leq 0.4$ when the nominal resolution was used. In all other cases, the twist-and-shift boundary was used and $\hat{s} \neq 0$. For the parallel extent of the flux tube, only one poloidal turn was simulated for each radial position. With $1.09 \leq |q| \leq 1.16$ for all considered radial positions, about one full toroidal turn was simulated in each flux tube position.

The ion-scale kinetic-electron high-resolution simulations proved to be extremely computationally expensive. As such, only two positions for the four scenarios were checked. Since the edge region significantly influences the plasma profiles, $\hat{\rho} = 0.7$ was chosen as the first point. Next, to introduce variation to this test, $\hat{\rho} = 0.4$ was selected as

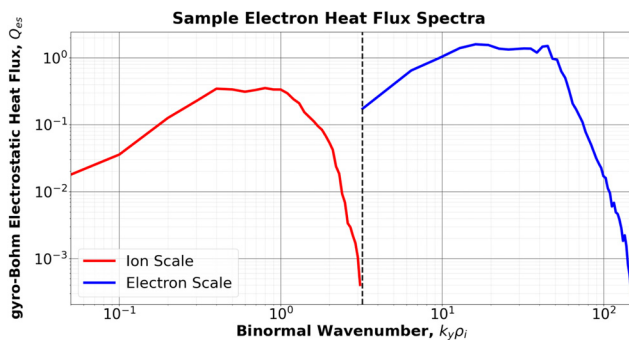


FIG. 4. Combined electrostatic heat flux spectra for electrons. The electron-scale spectra also begins at $k_y \rho_i = 0$, but this point was omitted from the plot.

the second point. This position lies sufficiently distant from both the edge region, which is already represented by the $\hat{\rho} = 0.7$ simulation, and the magnetic axis, which is generally less interesting from a simulation viewpoint as mentioned earlier. For both positions, good agreement between the nominal- and high-resolution fluxes at both the ion- and electron-scales is observed for all four scenarios. This result confirms that the nominal resolution parameters were indeed acceptable.

V. SIMULATION RESULTS

The experimental data points and the statistical fits are shown in Fig. 5. For the rest of Sec. V, the statistical fit for the temperature profiles will no longer be shown to simplify the plots. The electron density (n_e) profiles were obtained through an interferometer⁴³ and a Thomson scattering system.⁴⁴ The Thomson scattering system was also used to obtain the electron temperature (T_e) profiles. Finally, the ion temperature (T_i) profiles were measured using an x-ray imaging crystal spectrometer (XICS)^{45,46} and a charge exchange recombination spectroscopy system (CXRS).⁴⁷ A systematic bias was found for the former, but applying a correction for this improved the agreement between the XICS and CXRS measurements.¹⁷ The error bars of the data provides leeway for the simulated profiles to be adjusted by Tango while still allowing the experimental data to be adequately matched. For the first three phases of the workflow, the T_e , T_i , and n_e values at $\hat{\rho} = 0.8$ were used and kept fixed. In the fourth phase, where the density profiles were allowed to evolve, the impact of adjustments to the boundary conditions was explored.

Several questions were also explored and addressed in each phase. In phase 1, what is the relative contribution of ion- and electron-scale turbulence to the heat fluxes for each scenario? Moreover, how different are the heat fluxes for different flux tubes located on the same surface? In phase 2, how large are the neoclassical heat fluxes? Moreover, how do the neoclassical heat fluxes vary from one position to another? In phase 3, how significant is the reduction in the heat fluxes due to the neoclassical $E_r \times B$ shear? Finally, in phase 4, what are the parameters that affect the particle flux the most?

The next subsections will focus exclusively on the low-density ECRH scenario. The trends from other cases will be presented only when significant differences arise among the four. In phase 4, which is the culmination of the validation study simulations, the results will be shown for all four scenarios. Following this, selected turbulence characteristics and trends extracted from the simulations will be compared with those obtained from the experimental data.

A. Phase 1: Fixed density profile, without KNOSOS

In the beginning of this phase, the electron-scale simulation was first removed from the iteration loop. This was done for the low-density ECRH case to check the effect of electron-scale turbulence on the converged plasma profiles. The power balance was satisfied within 30 iterations. However, the T_e profile shown in Fig. 6 deviated significantly from the experimental data, especially for $\hat{\rho} \leq 0.5$. This was not surprising, given that the electron-scale heat fluxes could be significant for $\hat{\rho} \leq 0.5$. For this case, the contribution to the total electron heat flux Q_e in this range can be as high as 80%, as shown in Fig. 7(a). This is equivalent to 40% of the total heat flux. The sharp increase in the electron-scale flux contribution between $\hat{\rho} = 0.2$ and 0.3 is attributed to the significant increase in the normalized electron temperature

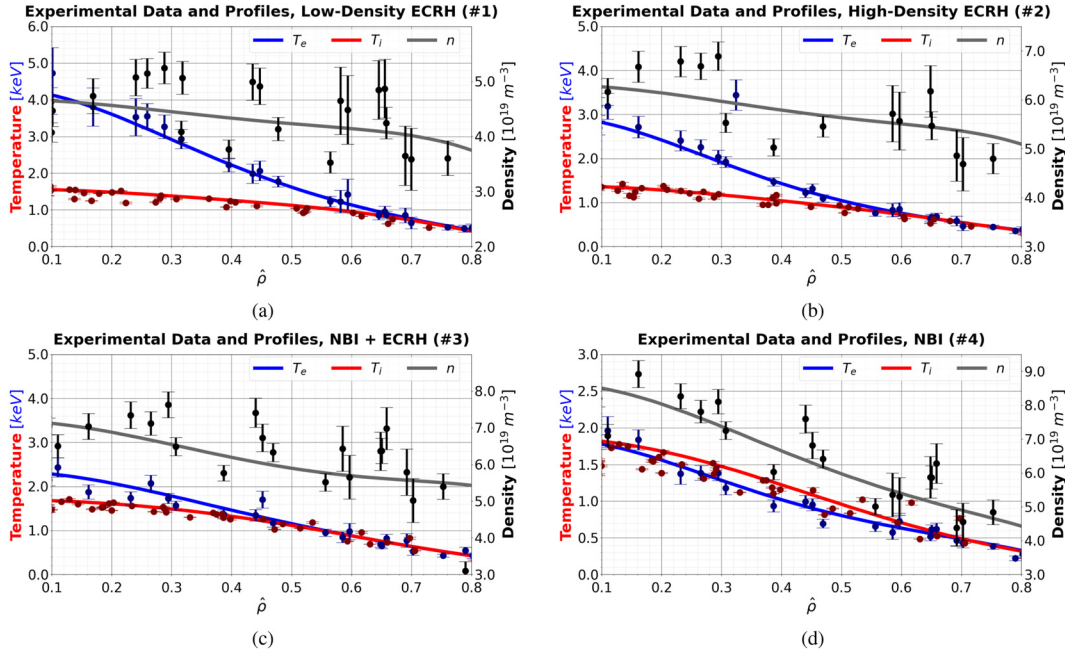


FIG. 5. The experimental data points and the statistical fits, which were used as the initial profiles for the simulation framework, for the (a) low-density ECRH, (b) high-density ECRH, (c) NBI + ECRH, and (d) NBI scenarios.

Phase 1 Temperature Profiles, Low-Density ECRH (#1)

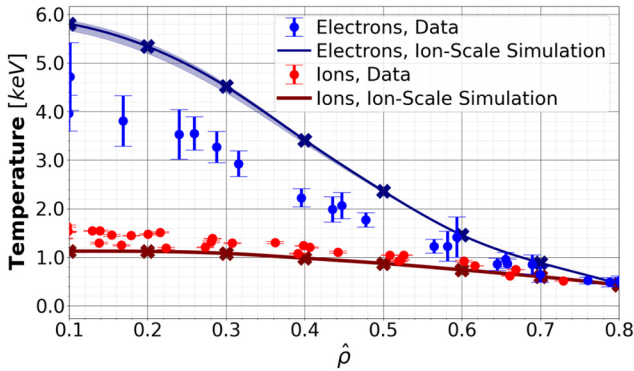


FIG. 6. Temperature profiles for the low-density ECRH case without the electron-scale simulation. The mean, minimum, and maximum from the last several iterations are shown.

gradient ω_{Te} by about 33%. In the absence of this heat loss channel, T_e would indeed increase. This result already highlights the importance of including electron temperature gradient (ETG) turbulence in modeling experiments, especially for electron-heated plasmas. The high-density ECRH and NBI + ECRH cases exhibited similar electron-scale heat flux contributions for $\hat{\rho} \leq 0.5$. The least contribution was observed for the NBI case, as depicted in Fig. 7(b), where the electron-scale heat flux amounted to 10%–25% of Q_e .

With the inclusion of electron-scale turbulence, good agreement between the simulated and experimental profiles was achieved, as seen in Fig. 8. The increase in electron heat flux lowered the T_e profile and

augmented the ion heating through collisional heat transfer. It may be tempting to stop at this point and immediately conclude that the GENE-KNOSOS-Tango framework does indeed work, but the simulations were still lacking several physics and, more importantly, the density profiles were still fixed.

To check the validity of the results thus far, simulations for different flux tubes on a single surface were also performed. This was done to gauge the variation of the heat flux magnitude with respect to the $\alpha = 0$ flux tube, which was where the simulations have all been carried out. For reference, this is the flux tube that passes through the out-board mid-plane of the bean-shaped cross section of W7-X. The position of $\hat{\rho} = 0.8$ was selected and flux-tube simulations were carried out for five additional field lines as denoted by the field line label α in Fig. 9. The field line label α covers $[0, \frac{2\pi}{5}]$ due to the fivefold symmetry of W7-X. The maximum error of the $\alpha = 0$ heat flux with respect to that of the other field lines was about 23%, while the difference to the mean was only 6%. Due to the stiff dependency of the fluxes on their respective gradient drive, choosing a different flux tube for the simulations would most likely still yield the same temperature profiles.

This verification is also part of the procedure to check the potential impact of global effects in the simulations. To clarify, global effects pertain to two distinct aspects: full-surface and radially global effects. In general, both influence the plasma profiles,⁴⁸ but their importance can be assessed *a priori*. The moderate variation of the heat fluxes in Fig. 9 implies that full-surface effects should only have a minor influence on the resulting plasma profiles. For radially global effects, we examine the parameter $\rho^* = \rho_{\text{gyro}}/a$ of each simulation, where ρ_{gyro} is the gyroradius of the reference species and a is the effective minor radius of the magnetic geometry. As ρ^* decreases, flux-tube simulations reproduce global simulation results with increasing accuracy.^{49,50} In the four W7-X

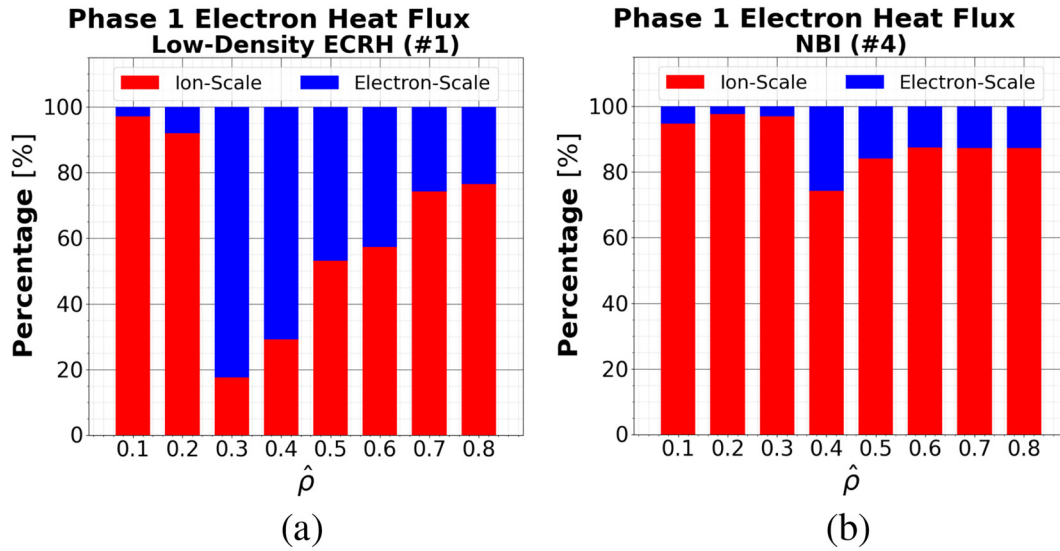


FIG. 7. Breakdown of electron heat fluxes for (a) low-density ECRH and (b) NBI scenarios.

Phase 1 Temperature Profiles, Low-Density ECRH (#1)

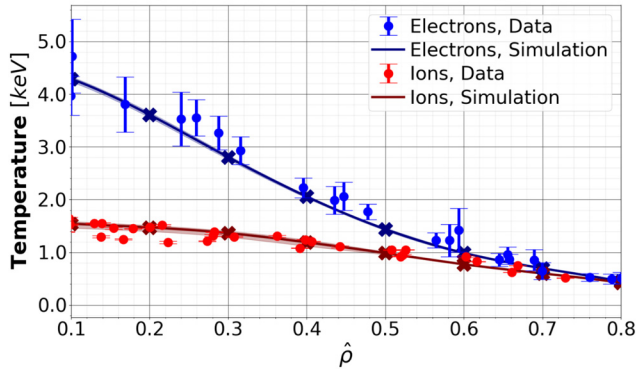


FIG. 8. Phase 1 temperature profiles for the low-density ECRH case. Both ion- and electron-scale simulations are present in the iteration loop.

scenarios, all ρ^* values were sufficiently small that radially global effects are expected to be minimal. These points support the conclusion that flux-tube simulations are sufficiently accurate for the purpose of profile prediction for our four W7-X scenarios. This approach is further reinforced by recent studies, which rely exclusively on flux-tube simulations for code validation and profile prediction.^{24,25,51–53}

B. Phase 2: Fixed density profile with neoclassical heat transport

With the addition of neoclassical heat transport, the temperature profiles decreased as seen in Fig. 10. The agreement worsened for the inner radial positions, especially for the electrons. On the other hand, the ions were less affected and exhibited a smaller temperature reduction. The breakdown of total electron and ion heat fluxes could explain these observations. In Fig. 11, it can be seen that the neoclassical

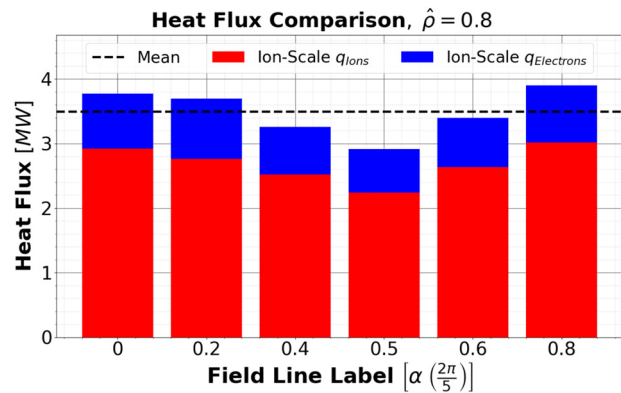


FIG. 9. Total turbulent heat fluxes for different flux tubes located on the same flux surface. The variation of the total heat flux among the flux tubes was moderate.

Phase 2 Temperature Profiles, Low-Density ECRH (#1)

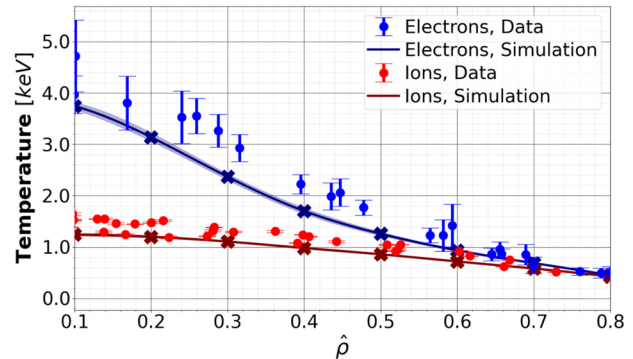


FIG. 10. Phase 2 temperature profiles for the low-density ECRH case. The addition of neoclassical heat fluxes caused a small reduction in the plasma temperatures.

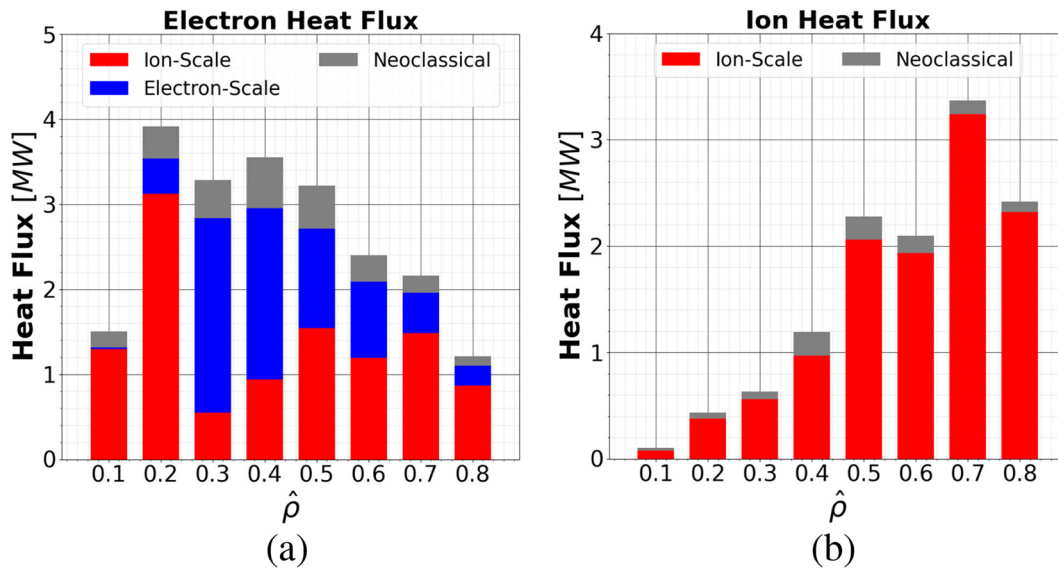


FIG. 11. Phase 2 flux breakdown for the (a) electron and (b) ions in the low-density ECRH case. The contribution of neoclassical heat flux is larger for the electrons.

electron fluxes of about 0.5 MW are relatively larger than those of the ions, with 0.1 MW on average. With a larger additional energy loss channel, the phase 1 electron temperature profile was flattened more by Tango to reduce the turbulent heat flux and maintain power balance.

The neoclassical heat fluxes Q_{neo} show good agreement with the KNOSOS-corrected calculations made using NEOTRANS⁵⁴ and DKES⁵⁵ mono-energetic coefficients.²⁶ The maximum was generally found in $0.3 \leq \hat{\rho} \leq 0.6$, with Q_{neo} gradually decreasing as one moved away from this range in either direction. The simulated neoclassical

flux profiles were generally more skewed toward $\hat{\rho} = 0.3$, which are in good agreement with the results shown in Ref. 26.

C. Phase 3: Fixed density profile with neoclassical heat transport and neoclassical $E_r \times B$ shear

In Fig. 12, the heat flux breakdown in gyro-Bohm units at each $\hat{\rho}$ is shown for phases 2, which included neoclassical transport but not the neoclassical $E_r \times B$ shear yet, and 3, where the shear was added to

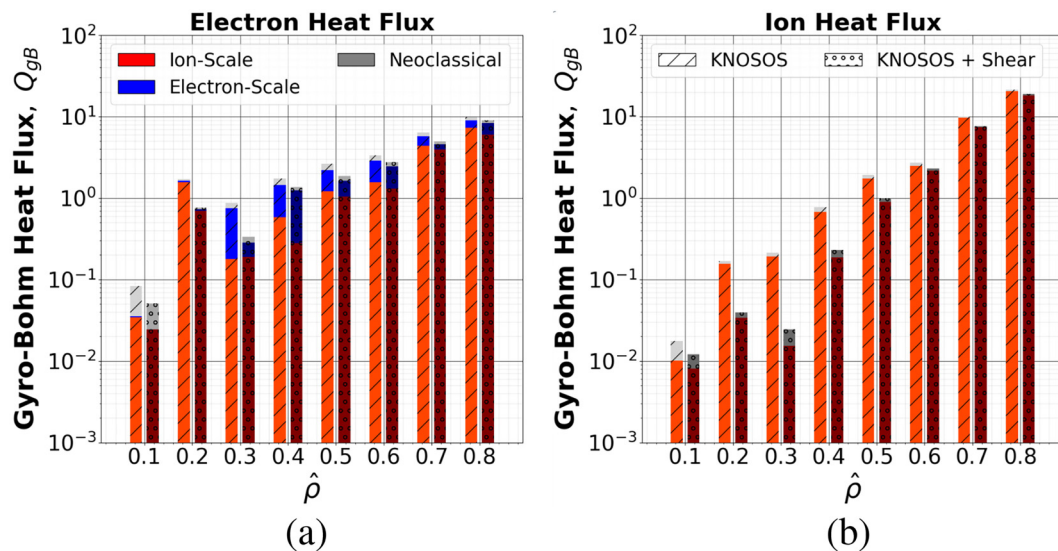


FIG. 12. Comparison of the gyro-Bohm (a) electron and (b) ion heat flux breakdown between phases 2 and 3 for the low-density ECRH case. The inclusion of the shear reduced the heat fluxes, especially the ion-scale contribution.

the GENE simulations. The side-by-side comparison shows that the heat fluxes were reduced as a result of this effect. First, the ion-scale heat fluxes were more impacted by the addition of neoclassical $E_r \times B$ shear. Physically, large-scale flows can have a large impact on turbulent transport. Radially varying, or sheared, flows disrupt turbulent structures and shorten their correlation lengths. Consequently, the distances over which heat and particles are transported are also reduced. Since shear diminishes the size of turbulent structures and eddies in the system, ion-scale structures were subjected to a larger reduction than those on the electron-scale, which are already relatively smaller to begin with. Comparison of gyro-Bohm heat fluxes between the second and third phases of the workflow show that a normalized neoclassical $E_r \times B$ shear, $\hat{\gamma}_E$, of 0.04 can already cause a 30%–50% reduction in the heat flux. The effect is not linear; a different $\hat{\gamma}_E$ does not necessarily impact the heat flux proportionally, especially under different plasma conditions.

Next, the low-density ECRH case exhibited a significant reduction of heat flux at $0.2 \leq \hat{\rho} \leq 0.4$, something that is not

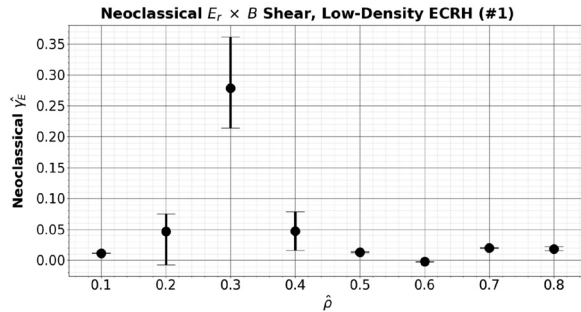


FIG. 13. Simulated $E_r \times B$ profile for the low-density ECRH scenario. The large shear at $\hat{\rho} = 0.3$ is due to an electron-ion root transition.

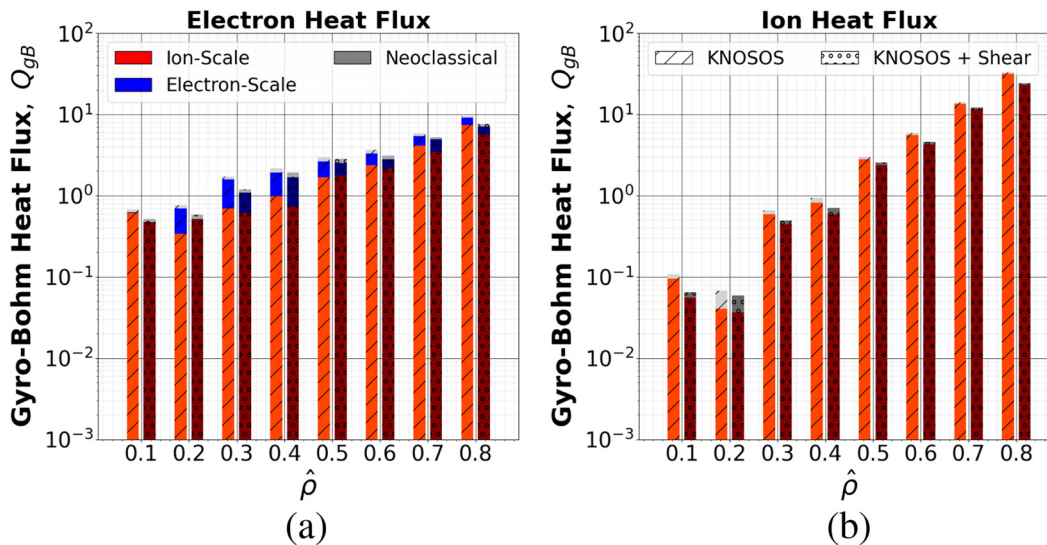


FIG. 14. Comparison of the gyro-Bohm (a) electron and (b) ion heat flux breakdown between phases 2 and 3 for the high-density ECRH case. No electron-ion root transition occurs at any of the flux-tube positions.

observed in the other scenarios. This is due to an electron-ion root transition^{56,57} occurring within this region, where the neoclassical E_r changes signs from positive to negative. Figure 13 depicts the $\hat{\gamma}_E$ profile for the low-density ECRH case. The position of the root transition shifted about $\hat{\rho} = 0.3$ as Tango modified the plasma profiles at every iteration, leading to relatively larger error bars for $\hat{\gamma}_E(0.2 \leq \hat{\rho} \leq 0.4)$. When $\hat{\gamma}_E$ is smaller, due to the absence of a root transition at the position of the flux tubes for instance, the heat flux reduction is less. Figure 14 illustrates this for the high-density ECRH case.

Due to this turbulence-suppressing effect, the temperature profiles increased with the inclusion of the shear. The agreement with experimental temperature data improved with respect to phase 2. Both experimental temperature profiles were recovered well by the simulations, as seen in Fig. 15. However, in some cases, T_e can be slightly higher in the inner radial region than the experimental data, such as in the NBI scenario.

D. Phase 4: Varying density profile with neoclassical heat transport and neoclassical $E_r \times B$ shear

Similar to phase 1, the experimental fit of the density data is used as the initial guess for the GENE and KNOSOS simulations. The boundary values of the temperature and density profiles from the statistical fit were initially used and kept fixed but adjustments were eventually made, as discussed later in this sub-section.

1. Fixed profile boundaries with $n_{0,edge} = 10^{13} \text{ m}^{-3}$

Several complications were encountered in this phase. First, the low- and high-density ECRH cases could not match the particle flux Γ at all positions consistently. Small changes in the plasma profiles led to large swings in the magnitude and sign of Γ , while some positions persistently had a negative total Γ . To remedy this convergence problem in the particle balance, two points, specifically $\hat{\rho} = 0.55$ and 0.75 , were

Phase 3 Temperature Profiles, Low-Density ECRH (#1)

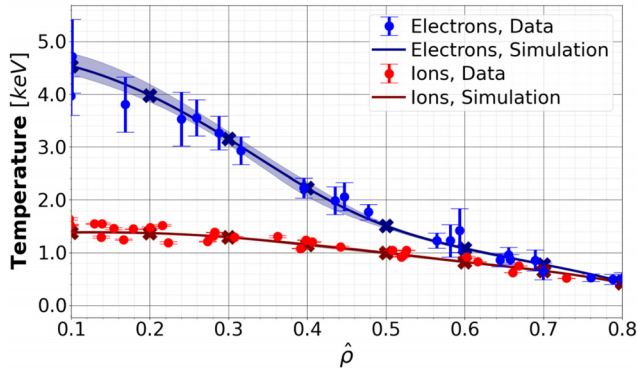


FIG. 15. Phase 3 temperature profiles for the low-density ECRH case. Good agreement with the experimental temperature data was recovered relative to phase 2.

added for the low- and high-density ECRH cases. The two ECRH particle balances consequently improved. For the two NBI scenarios, significant errors persisted near the boundary due to the limited number of flux tube positions in each iteration. The dotted lines,

signifying the mean flux radial profiles, had been essentially achieved with 30–40 iterations. Additional iterations with less Tango relaxation ($w = 0.6$) did not improve the balances. Adding extra flux tubes, similarly at $\hat{\rho} = 0.55$ and 0.75 for example, might have helped but was not pursued because the stiff relationship between fluxes and profiles suggested little benefit. Plasma profiles changed minimally between iterations, despite relatively larger flux value swings for $\hat{\rho} \geq 0.6$. Furthermore, the NBI cases already satisfied the balances well for $\hat{\rho} \leq 0.6$, making additional iterations with more radial positions less appealing. The final results for all four scenarios are shown in Figs. 16 and 17.

Disagreements are present between the experimental data and simulated plasma profiles. Although the two ECRH cases showed satisfactory agreement with several profile data points, the same could not be said for the two NBI cases. The T_e , T_i , and n_e profiles shown in Figs. 17(c), 17(d), 17(g), and 17(h) diverged from the experimental data. This was more pronounced for the density profiles, especially in the inner positions. Tango determined that a higher density gradient was necessary toward the edge of the radial domain, at $0.5 \leq \hat{\rho} \leq 0.8$. This resulted from encountering negative or inward Γ at these positions. More specifically, for the first iteration of phase 4 or the standalone simulation, the total Γ at $\hat{\rho} \geq 0.5$ were immediately negative for all four scenarios. This result was not

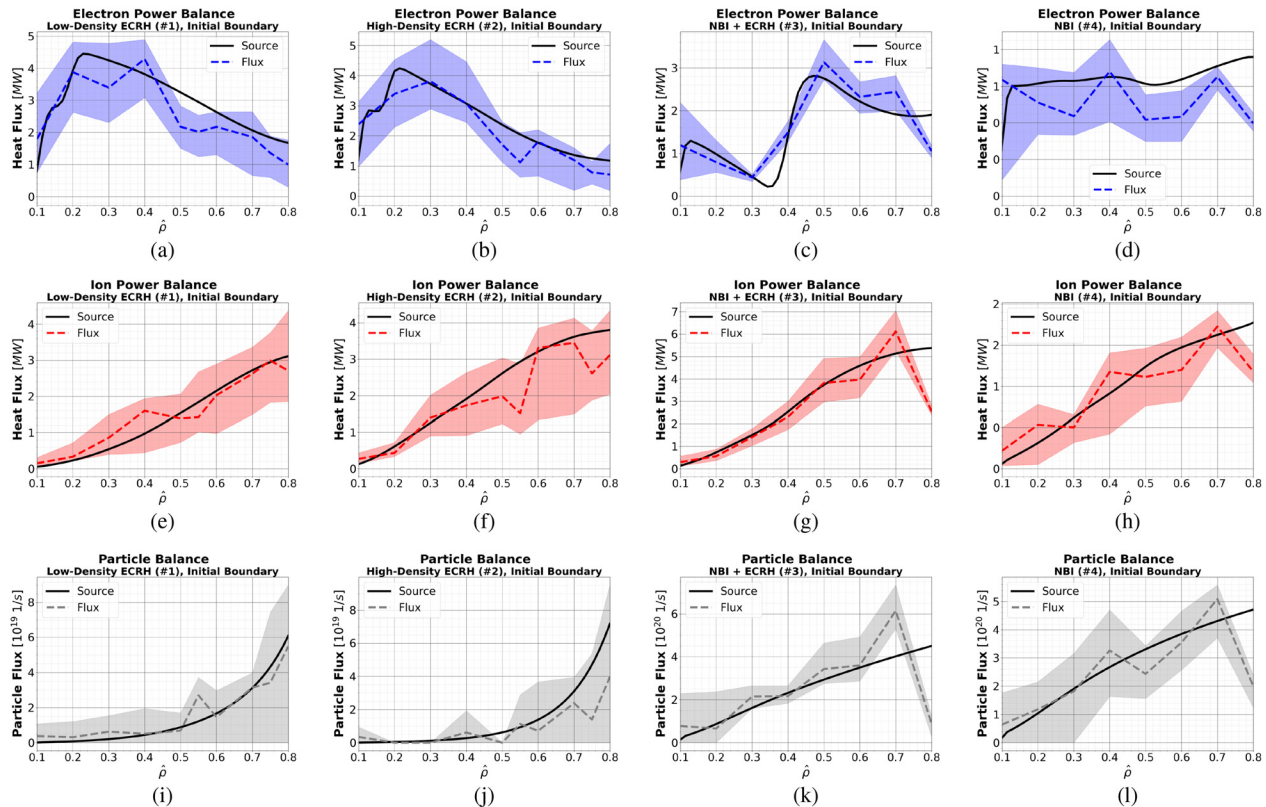


FIG. 16. Power and particle balances of the low-density ECRH (a), (e), and (i), high-density ECRH (b), (f), and (j), NBI + ECRH (c), (g), and (k), and NBI (d), (h), and (l) scenarios using the boundaries of the profile data fits. Two points, specifically $\hat{\rho} = 0.55$ and 0.75 , were added for the low- and high-density ECRH cases due to convergence problems in the particle balance.

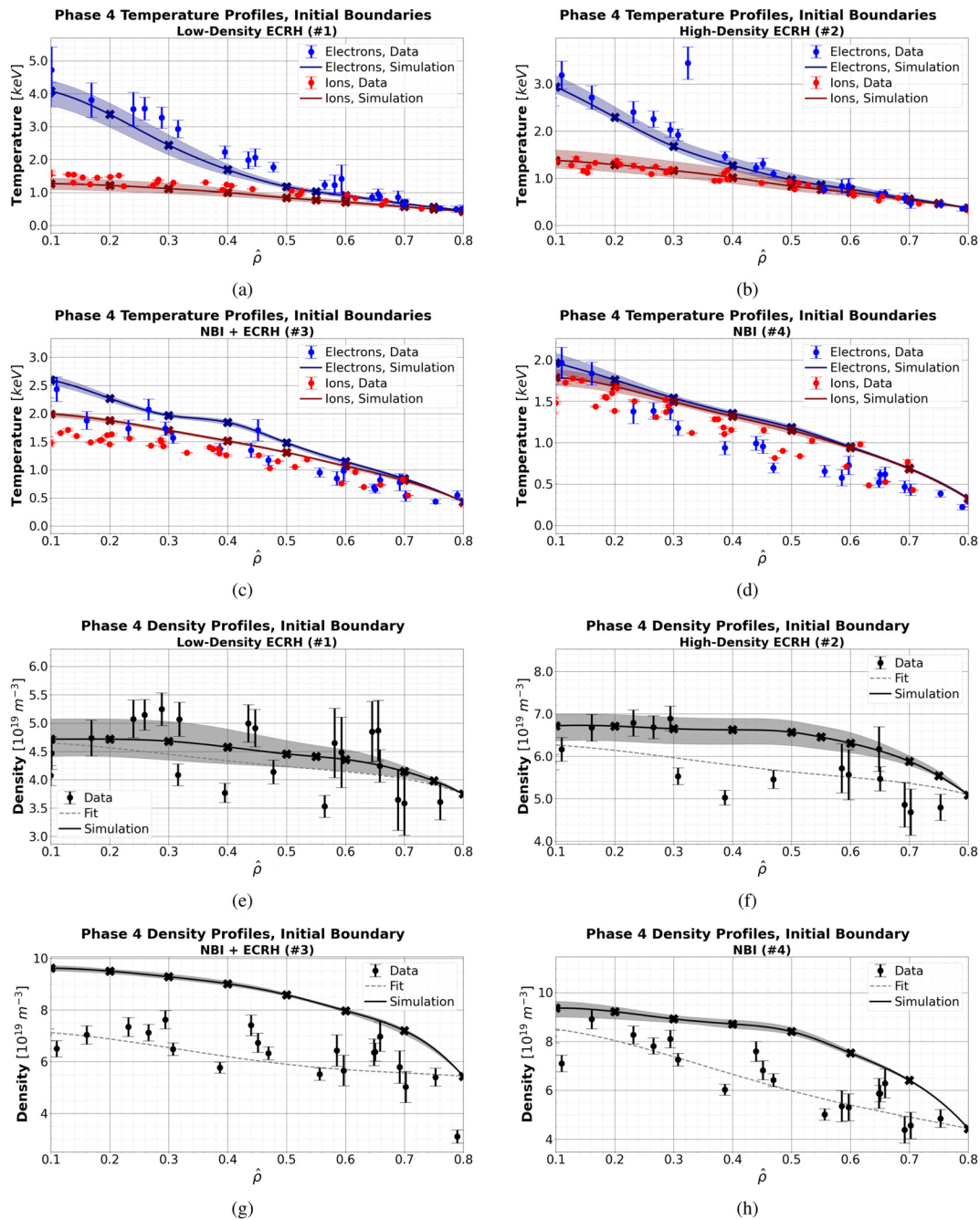


FIG. 17. Converged temperature and density profiles of the low-density ECRH (a) and (e), high-density ECRH (b) and (f), NBI + ECRH (c) and (g), and NBI (d) and (h) scenarios using the boundaries of the profile data fits. Agreement with the experimental data could be improved, especially for the two NBI scenarios as seen in (c), (d), (g), and (h).

compatible with the positive particle sources at these positions coming from neutrals ionization and/or NBI fueling. To recover total positive Γ from the KNOSOS and GENE simulations, Tango increased the density gradient at $\hat{\rho} \geq 0.5$. On the other hand, to

match the negligible Γ in the inner radial positions, it was flattened for $\hat{\rho} \leq 0.3$. This is consistent with the requirement of having large positive turbulent Γ for $\hat{\rho} \geq 0.5$ to compensate for the smaller neo-classical Γ in this region.³³

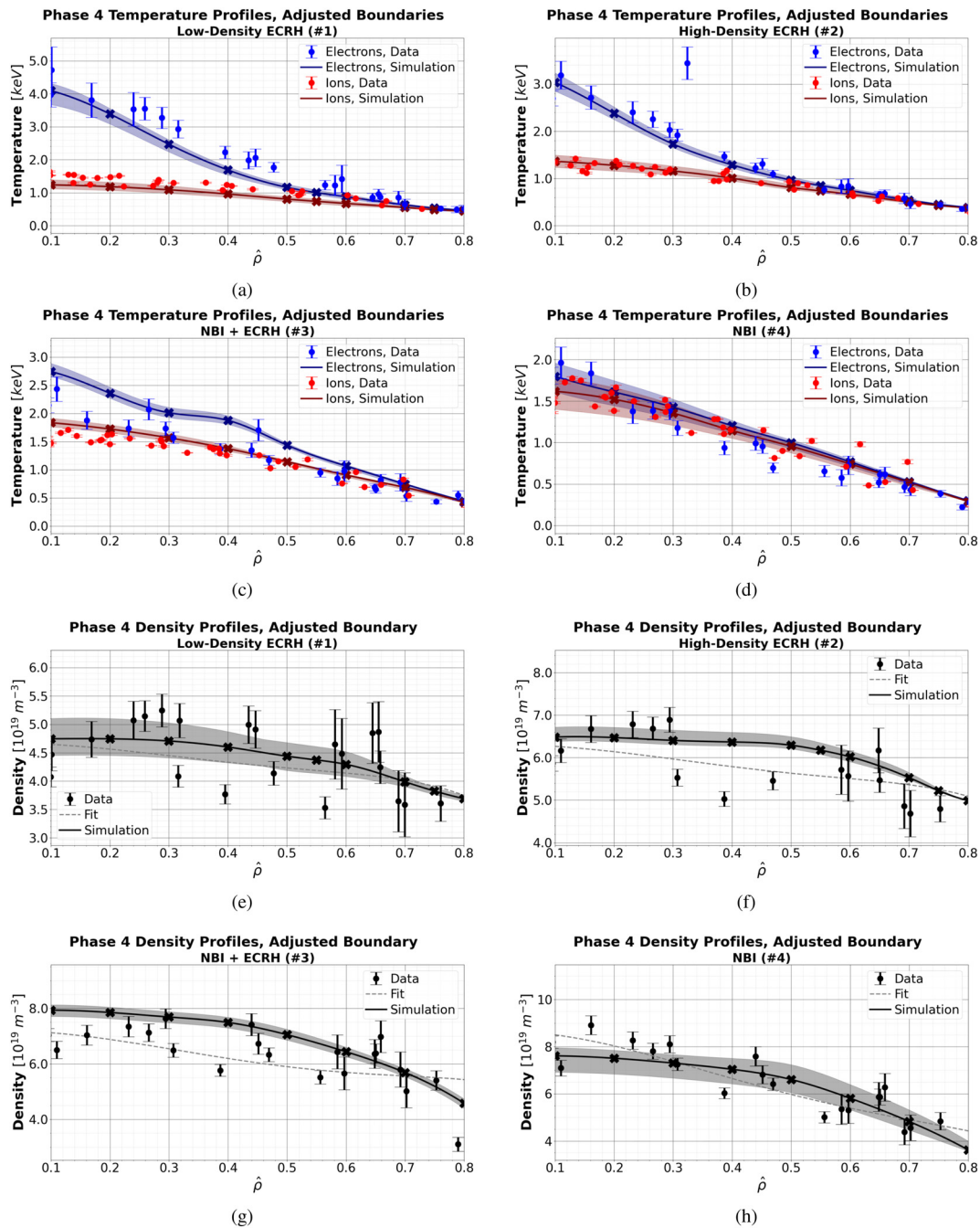


FIG. 18. Converged temperature and density profiles of the low-density ECRH (a) and (e), high-density ECRH (b) and (f), NBI + ECRH (c) and (g), and NBI (d) and (h) scenarios with adjusted temperature and density boundaries. Better agreement with the experimental data was achieved for all cases.

2. Adjusted profile boundaries with $n_{0,\text{edge}} = 10^{13} \text{ m}^{-3}$

Several options were available to improve the agreement of the simulated plasma profiles with the experimental data points. A separate study has been started due to the aforementioned prevalence of negative Γ in the outer half of the simulated radial domain. In addition

to the density gradient, it was found in this other study that the other primary factor dictating the sign of Γ is the collision frequency ν_c . The exact mechanism on how ν_c impacts Γ depends on several factors, such as profile gradients and the instabilities present in the plasma. More details will be provided in a different publication but one of the

key takeaways is that Γ becomes positive for sufficiently low values of ν_c . Given the linear relationship between ν_c and n_e , one possible adjustment to the density profile was to lower the boundary n_e . This was expected to reduce the collision frequency for all flux-tube simulations since the edge conditions dictate the core profile.¹⁹ In other words, to the zeroth order, moving the boundary density by a certain fraction will cause the rest of the profile to move by a similar magnitude. This would then give Tango a larger leeway in adjusting the density while simultaneously allowing the profile to stay close to the data points. Another possible adjustment was to increase the boundary T_e . Stemming from the inverse quadratic relationship between T_e and ν_c , smaller adjustments in T_e are enough to reproduce the reduction in ν_c by decreasing the boundary n_e .

These adjustments were the focus of the second batch of phase 4 simulations. The simulations were initialized using the converged plasma profiles from phase 3. Instructions were then provided to Tango to gradually adjust the temperature and density boundaries. The adjustment rate of a boundary condition was limited by the relaxation parameter w . The fulfilment of particle and power balances and the agreement of the simulated profiles with the experimental data were manually assessed a few iterations after every new set of boundary values had been reached.

From Fig. 18, it can be seen that small boundary adjustments within the error bars can have a significant effect on the inner core profiles, allowing for better matching of the experimental data points and compliance of power and particle balances. This emphasizes the importance of the plasma edge, which is unfortunately beyond the scope of this study. The fitted density profiles are shown in dotted gray lines, to facilitate comparison with the converged density profiles from the GENE-KNOSOS-Tango simulations. The earlier remark regarding the necessity of the larger density gradients at the boundary is clearly seen and confirmed by these second batch of phase 4 simulations.

3. Adjusted profile boundaries with $n_{0,edge} = 10^{14} \text{ m}^{-3}$

Despite these adjustments to the profiles, the sensitivity of Γ to small changes in the profiles for the low- and high-density ECRH cases still remained. This is apparent from Figs. 19(i) and 19(j), where Γ still covered the whole region under the particle source curves rather than being confined to a small region close to the curves. In contrast, the two NBI cases had Γ profiles that are consistently positive and matched the particle sources. It was hypothesized that this sensitivity stemmed from the difference in magnitudes of the particle sources, as

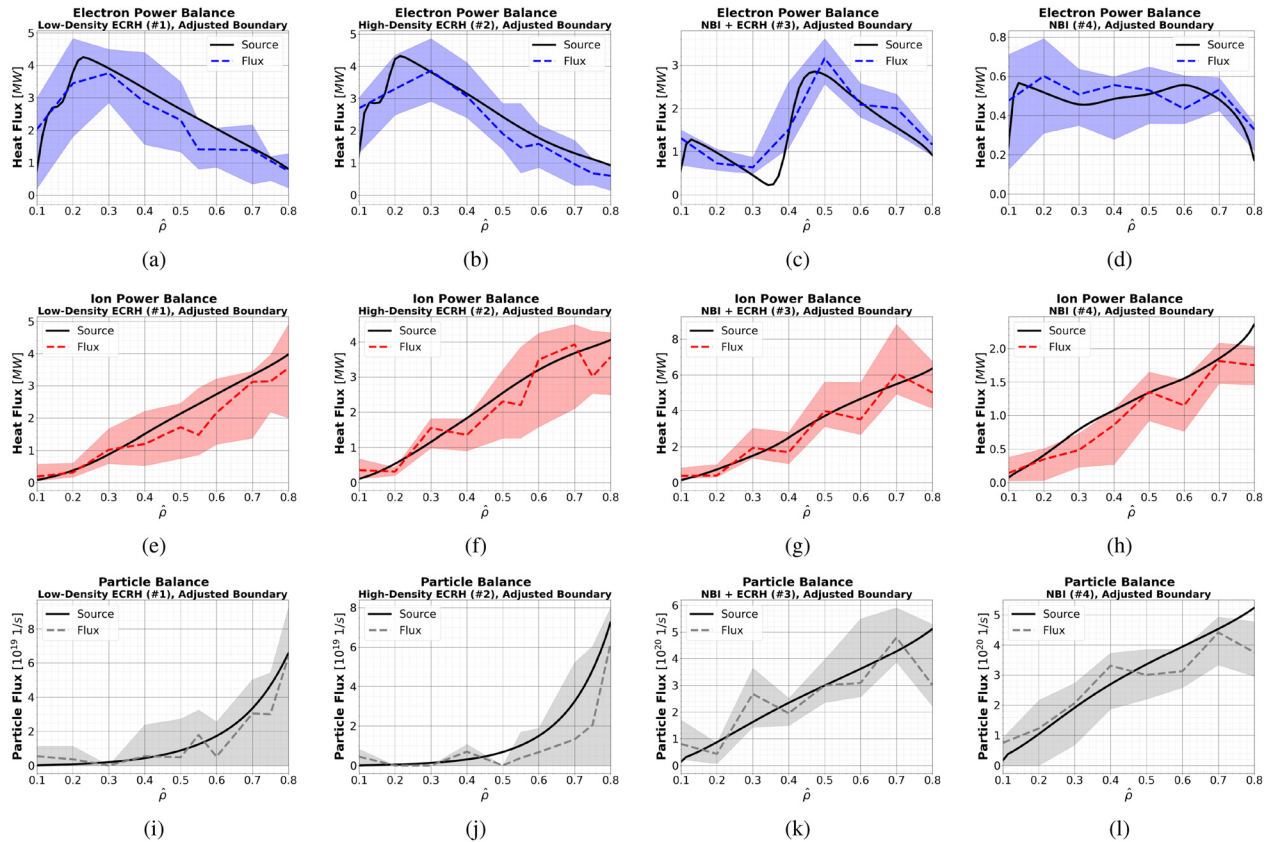


FIG. 19. Power and particle balances of the low-density ECRH (a), (e), and (i), high-density ECRH (b), (f), and (j), NBI + ECRH (c), (g), and (k), and NBI (d), (h), and (l) scenarios with adjusted boundaries for the plasma profiles and $n_{0,edge} = 10^{13} \text{ m}^{-3}$. Fulfilment of the balances slightly improved, but the particle balances of the two ECRH cases (i) and (j) still vary significantly between successive iterations.

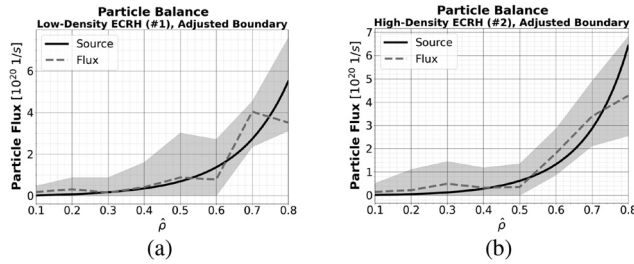


FIG. 20. Particle balances of the (a) low- and (b) high-density ECRH scenarios with adjusted boundaries for the plasma profiles and with an increased edge neutrals density of 10^{14} m^{-3} . Particle balances were more consistently matched, especially for $\hat{\rho} \geq 0.6$.

the source terms of the ECRH cases were both approximately one order of magnitude smaller than those of the NBI cases. This motivated the third batch of phase 4 simulations for the two ECRH cases, wherein $n_{0,edge}$ was increased to 10^{14} m^{-3} .

The two ECRH cases underwent an order of magnitude increase for their particle sources, significantly larger than the 75%–95% increase observed in the two NBI cases. Figure 20 shows the particle balances for cases 1 and 2, which were more adequately satisfied. Small adjustments were further needed for the boundary density and temperatures but, in general, the plasma profiles were comparable to those obtained with the $n_{0,edge} = 10^{13} \text{ m}^{-3}$ simulations of Sec. V D 2. In Table II, the boundary values before (“Fit”) and the mean values after adjustment (“Final”) are listed. The ion temperature T_i is not included in the table since $T_i \approx T_e$ at $\hat{\rho} = 0.8$.

With the particle balances sufficiently satisfied, we first examine the breakdown of the particle flux. Figure 21 shows this for the high-density ECRH scenario; similar trends are seen across the other cases. The neoclassical contribution peaks at $\hat{\rho} \leq 0.4$ before gradually declining toward the edge. The inward turbulent flux near the core is offset by the neoclassical component, which constitutes 50%–60% of the sum of the magnitudes. Near the edge, the neoclassical contribution falls to 10%–20%.

Building on this, we now revisit the breakdown of heat fluxes by scale for each scenario. Figure 22 depicts the breakdown for the two ECRH scenarios. The low- and high-density ECRH scenarios had large electron-scale contributions to the total electron heat flux, peaking at about 60% for both. As one moves radially outward, the electron-scale contribution first increased until $\hat{\rho} = 0.3$ followed by a gradual reduction toward the radial boundary. The upward trend is explained by the

TABLE II. Comparison of fitted and final values for n_e and T_e across the four scenarios. Cases 1, 2, 3, and 4 are the low-density ECRH, high-density ECRH, NBI + ECRH, and NBI scenarios, respectively.

Parameter	ECRH scenarios		NBI scenarios	
	Case 1	Case 2	Case 3	Case 4
Fit n_e (10^{19} m^{-3})	3.75 ± 0.40	5.09 ± 0.48	5.43 ± 0.50	4.43 ± 0.50
Final n_e (10^{19} m^{-3})	3.49 ± 0.29	4.56 ± 0.46	4.76 ± 0.65	3.62 ± 0.50
Fit T_e (keV)	0.45 ± 0.11	0.37 ± 0.06	0.43 ± 0.06	0.33 ± 0.06
Final T_e (keV)	0.46 ± 0.03	0.38 ± 0.05	0.43 ± 0.05	0.30 ± 0.05

Phase 4 Particle Fluxes
High-Density ECRH (#2), Adjusted Boundaries

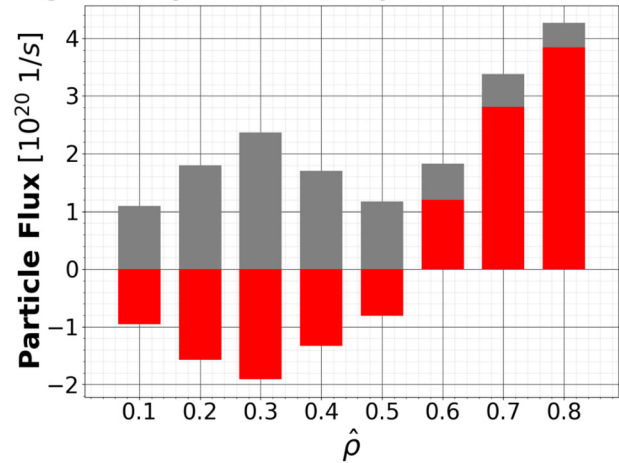


FIG. 21. Particle flux breakdown for the high-density ECRH case.

destabilization of the ETG mode by the increasing electron temperature gradient ω_{Te} and decreasing electron-ion temperature ratio $\tau = T_e/T_i$,⁵⁸ while the decreasing trend can be attributed to the steady increase in the density gradient ω_n with $\hat{\rho}$, which stabilizes the ETG mode.^{58–60}

On the other hand, the two NBI cases showed relatively less electron-scale contributions to the total electron heat flux, as seen in Fig. 23. The inverse dependence on $\hat{\rho}$ was still observed, but the peak percentage was reduced to approximately 40% and 20% for the NBI + ECRH and NBI scenarios respectively. For these two cases, where $T_i \sim T_e$ and $\omega_{Ti} \sim \omega_{Te}$, the ion-scale electron heat fluxes dominated; this is consistent with previous findings.⁶¹

After successfully reproducing the plasma profiles, the next step was to verify whether the turbulent properties derived from the simulations aligned with the observed experimental trends.

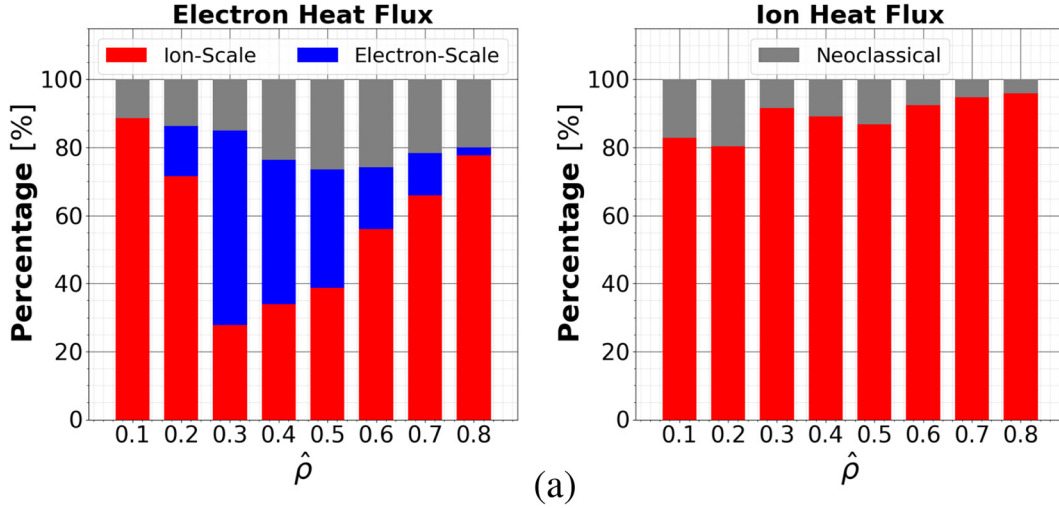
E. Comparison with selected experimental trends

It is important to note that the simulated turbulence trends were examined only at the end of each phase of the workflow. Therefore, the following results did not influence any of the simulations, especially for the final phase where the profile boundaries were adjusted. This approach ensured an unbiased check for the validation process to assess whether the combined results from the GENE and KNOSOS simulations could reproduce the turbulence trends obtained from the experimental data.

Three figures from Refs. 17 and 26 were chosen to be replicated using simulation results. First, in Fig. 24, the radial profiles of the total turbulent diffusivities $\chi_{(i+e)}$ for the four cases are illustrated. Good qualitative agreement with the experimental trend [Fig. 3(b) of Ref. 26] is evident. The two ECRH cases, the light and dark blue curves, indeed have roughly the same $\chi_{(i+e)}$ throughout the covered radial range. The NBI + ECRH scenario, the orange curve, has a crossover point at about $\hat{\rho} = 0.4$, where its $\chi_{(i+e)}$ exceeds that of the ECRH cases. Finally, the NBI scenario, the red curve, exhibits the lowest value among the four.

Figure 25 further builds upon this observation regarding the NBI scenario by comparing the ion turbulent diffusivity χ_i with the squared

Phase 4 Heat Flux for Low-Density ECRH (#1), Adjusted Boundaries



Phase 4 Heat Flux for High-Density ECRH (#2), Adjusted Boundaries

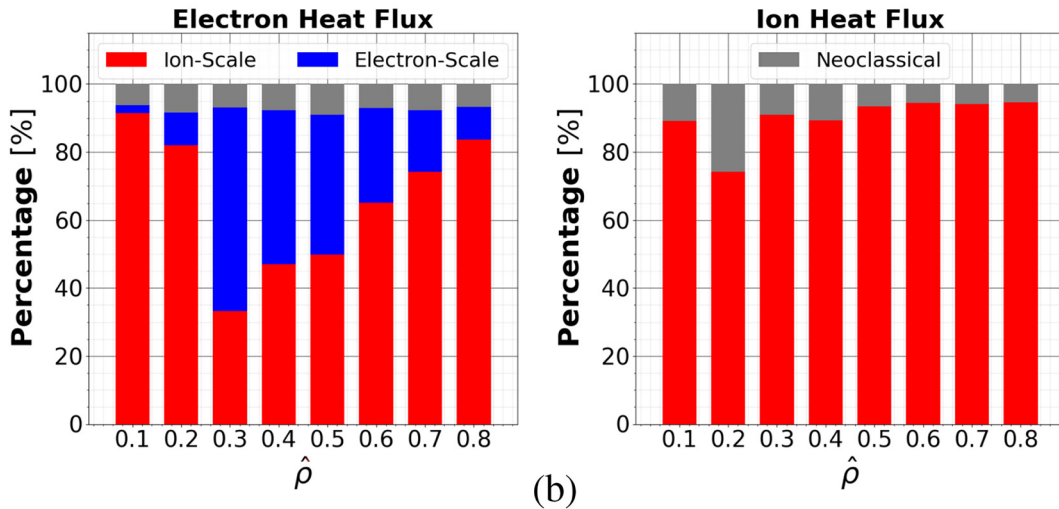


FIG. 22. Breakdown of electron and ion heat fluxes for the (a) low- and (b) high-density ECRH scenarios. The electron-scale heat fluxes significantly contributed to the electron total.

ion density fluctuations \tilde{n}_i^2 . During the W7-X discharges, a Doppler reflectometry diagnostic measures the backscattered power at the cutoff layer, which is approximately proportional to the square of the density fluctuations at $0.5 \leq \hat{\rho} \leq 0.75$.^{62,63} Spatial scales comparable to the ion gyroradius ρ_i , particularly $k_{\perp} \rho_i \simeq 1$ where k_{\perp} is the mode wavenumber in the binormal direction, are probed.²⁶ To make the comparison with the experimental data equivalent, a wavenumber filter was applied to the \tilde{n}_i^2 values from the simulations. In Fig. 25, the data points for the four scenarios cluster within specific regions of the $\chi_i - \tilde{n}_i^2$ phase space. Two specific branches for the collision frequency ν and for the parameter $\eta_i = L_n/L_{T_i}$, where L_n and L_{T_i} are the local gradient scales of n_e and T_i respectively, can be observed with the experimental data. The parameter η_i is used to gauge the onset of the ITG instability, the predominant form of turbulence in these scenarios.^{64,65} First, in

decreasing the ν value that is characteristic of the high-density ECRH case, we arrive at the low-density ECRH case. Notably, the turbulent transport level, as measured here with χ_i , stays roughly the same. On the other hand, the η_i branch illustrates that χ_i decreases as \tilde{n}_i^2 drops for the high-density ECRH, NBI + ECRH, and the NBI scenarios.

The simulations recovered these trends qualitatively. First, the results reinforce that varying ν between the two ECRH cases can have a negligible impact on turbulent transport, despite having very different \tilde{n}_i^2 . The flux-tube simulations recovered a 5-dB difference approximately between the \tilde{n}_i^2 magnitude of the two ECRH cases. This 5-dB disparity is a result of the differences in the plasma profiles of the two cases, which consequently gave way to a difference in the gyro-Bohm heat fluxes. While both scenarios have a heat flux of about 5 MW at $0.4 \leq \hat{\rho} \leq 0.6$, the ion gyro-Bohm heat flux of the high-density

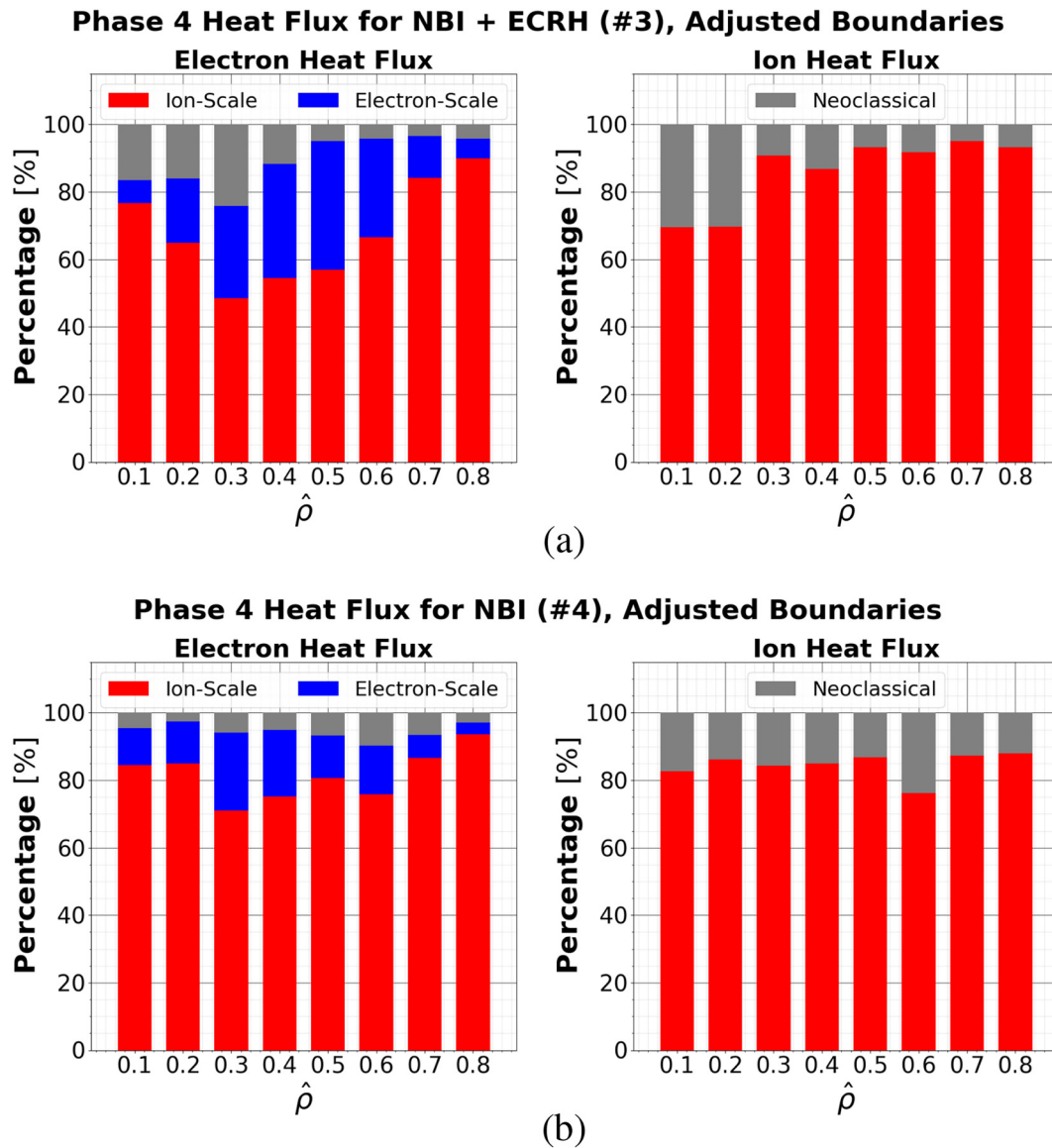


FIG. 23. Breakdown of electron and ion heat fluxes for the (a) NBI + ECRH and (b) NBI scenarios. The electron-scale heat fluxes accounted for relatively less when compared to the two ECRH scenarios.

ECRH case is about thrice of the low-density ECRH scenario's. Since the ion-scale density fluctuations are directly proportional to the ion gyro-Bohm heat flux, this difference primarily explains the simulated 5-dB difference.

The η_i branch reconstructed from the high-density ECRH, NBI + ECRH, and the NBI simulations mostly match well with the experimental χ_i values within the error bars. The simulations confirmed the experimental trend, where a reduction in η_i decreased the fluctuation amplitude arising from turbulence. Increasingly steeper density gradients for these three cases led to progressively higher degrees of ITG turbulence stabilization. The stabilization effect of η_i can still be observed in Fig. 26, where \tilde{n}_i^2 is plotted against η_i , when considering

the simulation and experimental data points for the high-density ECRH and NBI scenarios. More importantly, the simulations also successfully recovered the reduction in density fluctuations between the two ECRH scenarios despite the local gradients staying approximately the same.

While the \tilde{n}_i^2 trend is present qualitatively, there is some quantitative disagreement. The experiments showed a 10-dB difference between the \tilde{n}_i^2 of the two ECRH cases, which is equivalent to an order of magnitude. Within the context of the experiments, the leading theory for this is that the total fluctuation level actually stayed the same between the low- and high-density ECRH scenarios, but they only moved to a different location away from the Doppler reflectometry

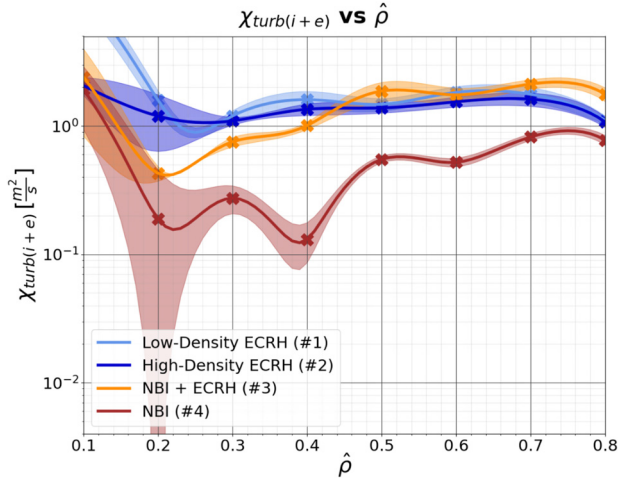


FIG. 24. Radial profile of the total turbulent heat diffusivity χ . The two ECRH and the NBI + ECRH cases have comparable χ , while the NBI case has the lowest χ among all four scenarios.

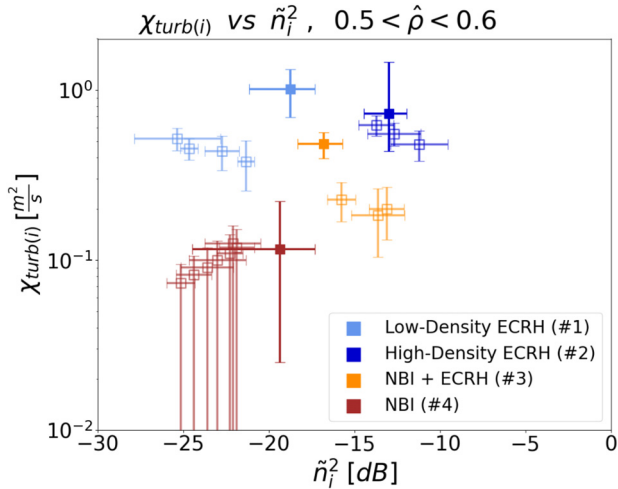


FIG. 25. Dependence of χ_i on the squared ion density fluctuations \tilde{n}_i^2 . The hollow translucent points are the experimental data, which are also shown in Fig. 3(c) of Ref. 26. The ν and η_i branches describe two turbulence trends that were successfully recovered by the simulations.

measurement zone.^{17,26,66} This resulted in the reduction of the measured fluctuation amplitude. This theory is difficult to confirm here due to the limitations of the flux-tube approach and can only be understood with simulations of higher fidelity. Full flux-surface and/or radially global simulations will be performed with GENE-3D in a separate study to verify this phenomenon.

VI. CONCLUSIONS AND OUTLOOK

In this study, we validated the GENE-KNOSOS-Tango simulation framework against four W7-X experimental scenarios. A

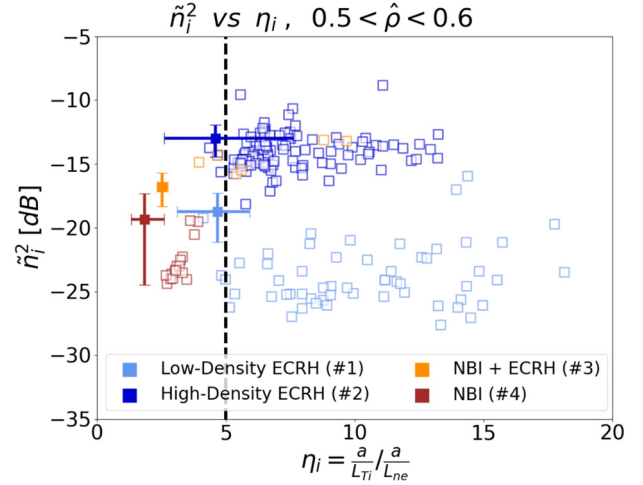


FIG. 26. Relationship between the squared ion density fluctuations \tilde{n}_i^2 and η_i .¹⁷ Good qualitative agreement is observed between the experiment and simulations. The hollow translucent points are the experimental data, which are also shown in Fig. 13 of Ref. 17. The quantitative discrepancy for the \tilde{n}_i^2 separation of the ECRH cases will be further studied.

workflow was adapted to divide the validation study into four phases. In the first phase, only GENE and Tango were iterating at each step, and the plasma density profile was kept fixed. Ion-scale kinetic-electron and electron-scale adiabatic-ion flux-tube simulations were each performed for eight radial positions to predict the plasma temperature profiles, given the heating power to the ions and electrons. In the second phase, neoclassical heat fluxes were included in the simulation loop through KNOSOS. In the third phase, the neoclassical $E_r \times B$ shear was calculated during each iteration and used as an additional input to GENE. Finally, in the fourth phase, the density profile was allowed to be varied.

In general, a good match between the experimental and simulated plasma profiles could be achieved. For the first three phases of the workflow, where the density profiles were kept fixed, the simulated temperature profiles remained within the experimental error bars while capturing the expected trends for the electron-scale heat flux contributions and neoclassical heat fluxes. The results of each phase also revealed some important findings. The heat flux variation over several flux tubes on the same surface was moderate, and this variation could not explain notable differences between experimental and simulated profiles for the considered cases. Second, electron-scale turbulence can be important and needs to be taken into account to match experimental profiles, especially for electron-heated plasmas. Next, the inclusion of neoclassical $E_r \times B$ shear decreases plasma turbulence, especially on the ion scale.

For the fourth phase, where the density profiles were allowed to evolve, the importance of boundary conditions became more pronounced. While using boundary conditions from experimental data curve fits yielded a satisfactory match of the simulated profiles with the profile data for the two ECRH cases, the two NBI cases required larger adjustments in the boundary values to allow the simulated profiles to align with the data. Another important parameter is the edge neutrals density $n_{0,edge}$, which dictates the particle source term via recycling and

ionization. The work shows that more accurate measurements of the density profiles and its gradient and of the neutral species density near the plasma boundary are necessary for a more thorough assessment of the particle transport model. Furthermore, this shows that proper modeling of the edge conditions is necessary for predicting plasma profiles across the entire radial domain.

Finally, the simulations qualitatively reproduced the experimental trends in turbulence characteristics, such as heat diffusivities χ and squared ion density fluctuations \tilde{n}_i^2 . In particular, they successfully captured the η_i branch of Fig. 25, where \tilde{n}_i^2 for the high-density ECRH, NBI + ECRH, and NBI scenarios decreases with η_i due to the stabilization of ITG turbulence. The ν branch of the high- and low-density ECRH scenarios was also recovered, suggesting that while the turbulent transport remained comparable, the fluctuations shifted to a different location on the flux surface. Furthermore, the reduction in \tilde{n}_i^2 is evident in Fig. 26, despite the two ECRH scenarios exhibiting similar local η_i . Though there are quantitative differences, the qualitative reproduction of experimentally observed trends using gyrokinetic simulations is already a promising result and an equally important aspect of the validation study.

Looking ahead, we identify several potential directions for this study to pursue. First, the studied radial domain can be extended to $0.8 < \hat{\rho} \leq 1.0$, which will necessitate the treatment of impurities as a trace species in the simulations. It will be interesting to understand how the inclusion of impurities will affect turbulent transport. Initially, radiation losses from impurities lower edge temperatures, increasing collisionality. The consequent reduction of the particle fluxes would lead to a steepening of the density profile. Then, a complex interplay between ITG stabilization by higher density gradients and the adjustment of temperature profiles would soon follow. Second, we plan to perform global GENE-3D simulations to analyze and better understand the simulated turbulence features. Our results already highlight some limitations of the flux-tube approach for studying turbulence fluctuations, especially for the low- and high-density ECRH scenarios. Synthetic diagnostics will be applied to the global simulations to enable a more detailed and robust validation against experimental turbulence measurements. Next, performing multi-scale simulations for these four cases is a possible path to take in order to determine if our findings regarding the persistence of electron-scale heat fluxes remain true and if there are interactions between the ion and electron scales. Finally, we will continue the validation study for other discharges beyond the parameter space covered here, such as the high-performance pellet fueling and high-beta scenarios.

ACKNOWLEDGMENTS

This work has been carried out within the framework of the EUROfusion Consortium, funded by the European Union via the Euratom Research and Training Programme (Grant Agreement No 101052200 — EURO-fusion) and by the Spanish Ministry of Science, Innovation and Universities (Grant No. PID2021-125607NB-I00). We acknowledge the EuroHPC Joint Undertaking for awarding this project access to the EuroHPC supercomputer LUMI, hosted by CSC (Finland) and the LUMI consortium through a EuroHPC Regular Access call. The simulations were completed under a project (Grant No. 465000821). Views and opinions expressed are however those of the author(s) only and do not necessarily reflect those of the European Union or the

European Commission. Neither the European Union nor the European Commission can be held responsible for them. Numerical simulations were performed at the Raven HPC system at the Max Planck Computing and Data Facility (MPCDF), Germany, the Marconi 100 & Leonardo Fusion supercomputer at CINECA, Italy, and the LUMI supercomputer at the CSC Data Center, Finland.

AUTHOR DECLARATIONS

Conflict of Interest

The authors have no conflicts to disclose.

Author Contributions

D. L. C. Agapito Fernando: Conceptualization (equal); Data curation (lead); Formal analysis (lead); Investigation (lead); Methodology (lead); Project administration (lead); Software (equal); Validation (lead); Visualization (lead); Writing – original draft (lead); Writing – review & editing (lead). **A. Bañón Navarro:** Conceptualization (equal); Formal analysis (supporting); Methodology (supporting); Project administration (supporting); Resources (equal); Software (supporting); Supervision (lead); Writing – review & editing (supporting). **D. Carralero:** Conceptualization (supporting); Data curation (supporting); Formal analysis (supporting); Investigation (supporting); Writing – review & editing (supporting). **A. Alonso:** Conceptualization (supporting); Methodology (supporting); Writing – review & editing (supporting). **A. Di Siena:** Conceptualization (supporting); Methodology (supporting); Software (supporting); Writing – review & editing (supporting). **J. L. Velasco:** Software (equal); Writing – review & editing (supporting). **F. Wilms:** Conceptualization (supporting); Methodology (supporting); Software (supporting); Writing – review & editing (supporting). **G. Merlo:** Conceptualization (supporting); Methodology (supporting); Resources (equal); Software (equal); Writing – review & editing (supporting). **F. Jenko:** Conceptualization (supporting); Funding acquisition (lead); Project administration (supporting); Resources (equal); Supervision (equal); Writing – review & editing (supporting). **S. A. Bozhnikov:** Data curation (supporting); Investigation (supporting). **E. Pasch:** Data curation (supporting); Investigation (supporting). **T. Windisch:** Data curation (supporting); Investigation (supporting). **G. Fuchert:** Data curation (supporting); Investigation (supporting). **K. J. Brunner:** Data curation (supporting); Investigation (supporting). **J. Knauer:** Data curation (supporting); Investigation (supporting). **A. Langenberg:** Data curation (supporting); Investigation (supporting). **N. A. Pablant:** Data curation (supporting); Investigation (supporting). **T. Gonda:** Data curation (supporting); Investigation (supporting). **O. P. Ford:** Data curation (supporting); Investigation (supporting); Writing – review & editing (supporting). **L. Vano:** Data curation (supporting); Investigation (supporting). **T. Estrada:** Data curation (supporting); Investigation (supporting). **E. Maragkoudakis:** Data curation (supporting); Investigation (supporting). **Wendelstein 7-X Team:** Data curation (supporting); Investigation (supporting).

DATA AVAILABILITY

The data that support the findings of this study are available from the corresponding author upon reasonable request.

REFERENCES

- ¹G. Xu, Z. Lu, D. Chen, and B. Wan, "A promising approach to steady-state fusion: High-temperature superconducting strong-field stellarator with precise omnigenity," *Innovation* **5**, 100537 (2024).
- ²T. Klinger, T. Andreeva, S. A. Bozhnikov, C. Brandt, R. Burhenn, B. Buttenschön, G. Fuchert, B. Geiger, O. Grulke, H. Laqua *et al.*, "Overview of first Wendelstein 7-X high-performance operation," *Nucl. Fusion* **59**, 112004 (2019).
- ³J. Candy, C. Holland, R. Waltz, M. Fahey, and E. Belli, "Tokamak profile prediction using direct gyrokinetic and neoclassical simulation," *Phys. Plasmas* **16**, 060704 (2009).
- ⁴M. Barnes, I. Abel, W. Dorland, T. Görler, G. W. Hammett, and F. Jenko, "Direct multiscale coupling of a transport code to gyrokinetic turbulence codes," *Phys. Plasmas* **17**, 056109 (2010).
- ⁵M. Honda, "Application of genetic algorithms to modelings of fusion plasma physics," *Comput. Phys. Commun.* **231**, 94–106 (2018).
- ⁶M. Honda and E. Narita, "Machine-learning assisted steady-state profile predictions using global optimization techniques," *Phys. Plasmas* **26**, 102307 (2019).
- ⁷A. Di Siena, A. Bañón Navarro, T. Luda, G. Merlo, M. Bergmann, L. Leppin, T. Görler, J. B. Parker, L. L. LoDestro, T. Dannert, K. Germaschewski, B. Allen, J. Hittinger, B. W. Dorland, G. W. Hammett, F. Jenko, and the ASDEX Upgrade Team, and the EUROfusion MST1 Team, "Global gyrokinetic simulations of ASDEX Upgrade up to the transport timescale with GENE-Tango," *Nucl. Fusion* **62**, 106025 (2022).
- ⁸A. Di Siena, R. Bilato, A. Bañón Navarro, M. Bergmann, L. Leppin, T. Görler, E. Poli, M. Weiland, G. Tardini, F. Jenko, the ASDEX Upgrade Team, and the EUROfusion MST1 Team, "Impact of supra-thermal particles on plasma performance at ASDEX Upgrade with GENE-Tango simulations," *Nucl. Fusion* **64**, 066020 (2024).
- ⁹F. Jenko, W. Dorland, M. Kotschenreuther, and B. Rogers, "Electron temperature gradient driven turbulence," *Phys. Plasmas* **7**, 1904 (2000).
- ¹⁰J. L. Velasco, I. Calvo, F. Parra, and J. M. García-Regaña, "KNOSOS: A fast orbit-averaging neoclassical code for stellarator geometry," *J. Comput. Phys.* **418**, 109512 (2020).
- ¹¹J. L. Velasco, I. Calvo, F. I. Parra, V. d'Herbemont, H. M. Smith, D. Carralero, and T. Estrada, and the Wendelstein 7-X Team, "Fast simulations for large aspect ratio stellarators with the neoclassical code KNOSOS," *Nucl. Fusion* **61**, 116013 (2021).
- ¹²A. I. Shestakov, R. H. Cohen, J. A. Crotinger, L. L. LoDestro, A. Tarditi, and X. Q. Xu, "Self-consistent modeling of turbulence and transport," *J. Comput. Phys.* **185**, 399 (2003).
- ¹³J. B. Parker, L. L. LoDestro, D. Told, G. Merlo, L. F. Ricketson, A. Campos, F. Jenko, and J. A. F. Hittinger, "Bringing global gyrokinetic turbulence simulations to the transport timescale using a multiscale approach," *Nucl. Fusion* **58**, 054004 (2018).
- ¹⁴M. Maurer, A. Bañón Navarro, T. Dannert, M. Restelli, F. Hindenlang, T. Görler, D. Told, D. Jarema, G. Merlo, and F. Jenko, "GENE-3D: A global gyrokinetic turbulence code for stellarators," *J. Comput. Phys.* **420**, 109694 (2020).
- ¹⁵F. Wilms, A. Bañón Navarro, G. Merlo, L. Leppin, T. Görler, T. Dannert, F. Hindenlang, and F. Jenko, "Global electromagnetic turbulence simulations of W7-X-like plasmas with GENE-3D," *J. Plasma Phys.* **87**, 905870604 (2021).
- ¹⁶M. N. A. Beurskens, S. A. Bozhnikov, O. P. Ford, P. Xanthopoulos, A. Zocco, Y. Turkin, J. A. Alonso, C. Beidler, I. Calvo, D. Carralero, T. Estrada, G. Fuchert, O. Grulke, M. Hirsch, K. Ida, M. Jakubowski, C. Killer, M. Krychowiak, S. Kwak, S. A. Lazerson, A. Langenberg, R. Lunsford, N. A. Pablant, E. Pasch, A. Pavone, F. Reimold, T. Romba, A. von Stechow, H. M. Smith, T. Windisch, M. Yoshinuma, D. Zhang, R. C. Wolf, and the Wendelstein 7-X Team, "Ion temperature clamping in Wendelstein 7-X electron cyclotron heated plasmas," *Nucl. Fusion* **61**, 116072 (2021).
- ¹⁷D. Carralero, T. Estrada, E. Maragkoudakis, T. Windisch, J. A. Alonso, M. Beurskens, S. A. Bozhnikov, I. Calvo, H. Damm, O. P. Ford, G. Fuchert, J. M. García-Regaña, N. A. Pablant, E. Sánchez, E. Pasch, J. L. Velasco, and the Wendelstein 7-X Team, "An experimental characterization of core turbulence regimes in Wendelstein 7-X," *Nucl. Fusion* **61**, 096015 (2021).
- ¹⁸A. Bañón Navarro, A. Di Siena, J. L. Velasco, F. Wilms, G. Merlo, T. Windisch, L. L. LoDestro, J. B. Parker, and F. Jenko, "First-principles based plasma profile predictions for optimized stellarators," *Nucl. Fusion* **63**, 054003 (2023).
- ¹⁹A. Bañón Navarro, G. Roberg-Clark, G. Plunk, D. L. C. Agapito Fernando, A. Di Siena, F. Wilms, and F. Jenko, "Assessing core ion thermal confinement in critical-gradient-optimized stellarators," *Phys. Plasmas* **31**, 062508 (2024).
- ²⁰N. Mandell, W. Dorland, and M. Landreman, "Laguerre–Hermite pseudo-spectral velocity formulation of gyrokinetics," *J. Plasma Phys.* **84**, 905840108 (2018).
- ²¹N. Mandell, W. Dorland, I. Abel, R. Gaur, P. Kim, M. Martin, and T. Qian, "GX: A GPU-native gyrokinetic turbulence code for tokamak and stellarator design," *J. Plasma Phys.* **90**, 905900402 (2024).
- ²²T. Qian, B. Buck, R. Gaur, N. Mandell, P. Kim, and W. Dorland, "Stellarator profile predictions using Trinity3D and GX," in *64th Annual Meeting of the APS Division of Plasma Physics, 17–21 October* (Bulletin of the American Physical Society, Spokane, Washington, 2022).
- ²³M. Landreman, H. M. Smith, A. Mollén, and P. Helander, "Comparison of particle trajectories and collision operators for collisional transport in nonaxisymmetric plasmas," *Phys. Plasmas* **21**, 042503 (2014).
- ²⁴N. Mandell, W. Dorland, F. Parra, T. Qian, J. Sachdev, and J. L. Velasco, "Stellarator profile prediction using the T3D+GX+KNOSOS multi-scale gyrokinetic framework," in *65th Annual Meeting of the APS Division of Plasma Physics, 30 October–03 November* (Bulletin of the American Physical Society, Denver, CO, 2023).
- ²⁵M. Zarnstorff, T. Qian, N. Mandell, and W. Dorland, "Confinement simulation of optimized stellarators," in *66th Annual Meeting of the APS Division of Plasma Physics, 07–11 October* (Bulletin of the American Physical Society, Atlanta, Georgia, 2024).
- ²⁶D. Carralero, T. Estrada, E. Maragkoudakis, T. Windisch, J. A. Alonso, J. L. Velasco, O. P. Ford, M. Jakubowski, S. A. Lazerson, M. N. A. Beurskens, S. A. Bozhnikov, I. Calvo, H. Damm, G. Fuchert, J. M. García-Regaña, U. Höfel, N. Marushchenko, N. A. Pablant, E. Sánchez, H. M. Smith, E. Pasch, and T. Stange, and the Wendelstein 7-X Team, "On the role of density fluctuations in the core turbulent transport of Wendelstein 7-X," *Plasma Phys. Controlled Fusion* **64**, 044006 (2022).
- ²⁷P. Helander, "On rapid plasma rotation," *Phys. Plasmas* **14**, 104501 (2007).
- ²⁸R. C. Wolf, Y. Baranov, X. Garbet, N. Hawkes, A. Peeters, C. Challis, M. de Baar, C. Giroud, E. Joffrin, M. Mantsinen, D. Mazon, H. Meister, W. Suttrop, K.-D. Zastrow, the ASDEX Upgrade Team, and Contributors to the EFDA-JET Workprogramme, "Characterization of ion heat conduction in JET and ASDEX Upgrade plasmas with and without internal transport barriers," *Plasma Phys. Controlled Fusion* **45**, 1757 (2003).
- ²⁹G. Pereverzev and G. Corrigan, "Stable numeric scheme for diffusion equation with a stiff transport," *Comput. Phys. Commun.* **179**, 579 (2008).
- ³⁰G. W. Hammett, W. Dorland, N. Loureiro, and T. Tatsuno, "Implementation of large scale $E \times B$ shear flow in the GS2 gyrokinetic turbulence code," in *48th Annual Meeting of the APS Division of Plasma Physics, 30 October–03 November* (Bulletin of the American Physical Society, Philadelphia, Pennsylvania, 2006).
- ³¹D. Told, "Gyrokinetic microturbulence in transport barriers," Ph.D. thesis (Universität Ulm, Munich, Germany, 2012).
- ³²R. Hazeltine, M. Calvin, P. Valanju, and E. Solano, "Analytical calculation of neutral transport and its effect on ions," *Nucl. Fusion* **32**, 3 (1992).
- ³³H. Thienpondt, J. M. García-Regaña, I. Calvo, J. A. Alonso, J. L. Velasco, A. González-Jerez, M. Barnes, K. Brunner, O. P. Ford, G. Fuchert, J. Knauer, E. Pasch, L. Vanó, and the Wendelstein 7-X Team, "Prevention of core particle depletion in stellarators by turbulence," *Nucl. Fusion* **5**, L022053 (2023).
- ³⁴R. Janev and J. Smith, *Atomic and Plasma–Material Interaction Data for Fusion* (International Atomic Energy Agency, 1993), Vol. 4.
- ³⁵R. Janev, D. Reiter, and U. Samm, "Collision processes in low-temperature hydrogen plasmas," (International Atomic Energy Agency, 1993).
- ³⁶T. Romba, F. Reimold, O. P. Ford, T. W. C. Neelis, P. Zs. Pölöskei, T. Klinger, and the Wendelstein 7-X Team, "Measurements of radial neutral density profiles from balmer- α emission in Wendelstein 7-X," *Plasma Physics and Controlled Fusion* **67**(5), 055045 (2025).
- ³⁷T. Kremeyer, R. König, S. Brezinsek, O. Schmitz, Y. Feng, V. Winters, L. Rudischhauser, B. Buttenschön, K. J. Brunner, P. Drewelow, E. Flom,

- G. Fuchert, Y. Gao, J. Geiger, M. Jakubowski, C. Killer, J. Knauer, M. Krychowiak, S. A. Lazerson, F. Reimold, G. Schlisio, H. Viebke, and the Wendelstein 7-X Team, "Analysis of hydrogen fueling, recycling, and confinement at Wendelstein 7-x via a single-reservoir particle balance," *Nucl. Fusion* **62**, 036023 (2022).
- ³⁸M. McMillan and S. A. Lazerson, "BEAMS3D Neutral Beam Injection Model," *Plasma Phys. Controlled Fusion* **56**, 095019 (2014).
- ³⁹S. A. Lazerson, O. P. Ford, C. Nührenberg, S. Äkäslompolo, P. Zs. Poloskei, M. Machielsen, P. McNeely, L. Vanó, N. Rust, S. A. Bozhnikov, T. W. C. Neelis, J. P. Graves, D. Pfefferlé, A. Spanier, D. Hartmann, N. Marushchenko, Y. Turkin, M. Hirsch, N. Chaudhary, U. Hoefel, T. Stange, G. Weir, N. A. Pablant, A. Langenberg, P. Traverso, P. Valson, J. Knauer, K. J. Brunner, E. Pasch, M. N. A. Beurskens, H. Damm, G. Fuchert, P. Nelde, E. Scott, U. Hergenhausen, A. Pavone, K. Rahbarnia, T. Andreeva, J. Schilling, C. Brandt, U. Neuner, H. Thomsen, M. Jakubowski, A. Ali, Y. Gao, H. Niemann, A. P. Sitjes, R. Koenig, R. C. Wolf, and the Wendelstein 7-X Team, "Validation of the BEAMS3D neutral beam deposition model on Wendelstein 7-X," *Nucl. Fusion* **60**, 076020 (2020).
- ⁴⁰S. A. Lazerson, D. Pfefferlé, M. Drevlak, H. M. Smith, J. Geiger, S. Äkäslompolo, P. Xanthopoulos, A. Dinklage, O. P. Ford, P. McNeely, N. Rust, S. A. Bozhnikov, D. Hartmann, K. Rahbarnia, T. Andreeva, J. Schilling, C. Brandt, U. Neuner, H. Thomsen, R. C. Wolf, and the Wendelstein 7-X Team, "Modeling and measurement of energetic particle slowing down in Wendelstein 7-X," *Nucl. Fusion* **61**, 096005 (2021).
- ⁴¹N. Marushchenko, Y. Turkin, and H. Maassberg, "Ray-tracing code TRAVIS for ECR heating, EC current drive and ECE diagnostic," *Comput. Phys. Commun.* **185**, 165 (2014).
- ⁴²A. Richardson, 2019 *NRL Plasma Formulary* (U.S. Naval Research Laboratory, Washington, DC, 2019).
- ⁴³K. Brunner, T. Akiyama, M. Hirsch, J. Knauer, P. Kornejew, B. Kursinski, H. Laqua, J. Meineke, H. Trimino Mora, and R. C. Wolf, "Real-time dispersion interferometry for density feedback in fusion devices," *J. Instrum.* **13**, P09002 (2018).
- ⁴⁴S. A. Bozhnikov, M. N. A. Beurskens, A. D. Molin, G. Fuchert, E. Pasch, M. Stoneking, M. Hirsch, U. Höfel, J. Knauer, J. Svensson, H. Trimino Mora, and R. C. Wolf, "The Thomson scattering diagnostic at Wendelstein 7-X and its performance in the first operation phase," *J. Instrum.* **12**, P10004 (2017).
- ⁴⁵J. Kring, N. A. Pablant, A. Langenberg, J. Rice, L. Delgado-Aparicio, D. Maurer, P. Traverso, M. Bitter, K. Hill, and M. Reinke, "In situ wavelength calibration system for the X-ray imaging crystal spectrometer (XICS) on W7-X," *Rev. Sci. Instrum.* **89**, 10F107 (2018).
- ⁴⁶N. A. Pablant, A. Langenberg, J. A. Alonso, M. Bitter, S. A. Bozhnikov, O. P. Ford, K. W. Hill, J. Kring, O. Marchuck, J. Svensson, P. Traverso, T. Windisch, Y. Yakusevitch, and the Wendelstein 7-X Team, "Correction and verification of x-ray imaging crystal spectrometer analysis on Wendelstein 7-X through x-ray ray tracing," *Rev. Sci. Instrum.* **92**, 043530 (2021).
- ⁴⁷O. P. Ford, L. Vanó, J. A. Alonso, J. Balduhn, M. N. A. Beurskens, C. Biedermann, S. A. Bozhnikov, G. Fuchert, B. Geiger, D. Hartmann, R. J. E. Jaspers, A. Kappatou, A. Langenberg, S. A. Lazerson, R. M. McDermott, P. McNeely, T. W. C. Neelis, N. A. Pablant, E. Pasch, N. Rust, R. Schroeder, E. R. Scott, H. M. Smith, T. Wegner, F. Kunkel, and R. C. Wolf, and the Wendelstein 7-X Team, "Charge exchange recombination spectroscopy at Wendelstein 7-X," *Rev. Sci. Instrum.* **91**, 023507 (2020).
- ⁴⁸F. Wilms, "GENE-3D simulations of plasma turbulence in stellarators," Ph.D. thesis, (Technische Universität München, Munich, Germany, 2024).
- ⁴⁹J. Candy, R. Waltz, and W. Dorland, "The local limit of globalgyrokinetic simulations," *Phys. Plasmas* **11**, L25–L28 (2004).
- ⁵⁰B. McMillan, X. Lapillonne, S. Brunner, and L. Villard, "System size effects on gyrokinetic turbulence," *Phys. Rev. Lett.* **105**, 155001 (2010).
- ⁵¹P. Rodriguez-Fernandez, N. Howard, and J. Candy, "Nonlinear gyrokinetic predictions of SPARC burning plasma profiles enabled by surrogate modeling," *Nucl. Fusion* **62**, 076036 (2022).
- ⁵²P. Rodriguez-Fernandez, N. Howard, A. Saltzman, L. Shoji, T. Body, D. Battaglia, J. Hughes, J. Candy, G. Staebler, and A. Creely, "Core performance predictions in projected SPARC first-campaign plasmas with nonlinear CGYRO," *Phys. Plasmas* **31**, 062501 (2024).
- ⁵³W. Guttenfelder, N. Mandell, G. Le Bars, L. Singh, A. Bader, K. Camacho Mata, J. Canik, L. Carbajal, A. Cerfon, N. Davila, W. Dorland, C. Hegna, C. Holland, D. Huet, M. Landreman, C. Lau, A. Malkus, B. Medasani, J. Morrissey, and J. Schmitt, "Predictions of core plasma performance for the Infinity Two fusion pilot plant," *J. Plasma Phys.* **91**, E83 (2025).
- ⁵⁴H. M. Smith, see <https://gitlab.mpcdf.mpg.de/smithh/neotransp> for "NEOTRANSF".
- ⁵⁵W. van Rij and S. Hirshman, "Variational bounds for transport coefficients in three-dimensional toroidal plasmas," *Phys. Fluids B: Plasma Phys.* **1**, 563–569 (1989).
- ⁵⁶M. Yokoyama, H. Maaßberg, C. Beidler, V. Tribaldos, K. Ida, T. Estrada, F. Castejon, A. Fujisawa, T. Minami, T. Shimozuma, Y. Takeiri, A. Dinklage, S. Murakami, and H. Yamada, "Core electron-root confinement (CERC) in helical plasmas," *Nucl. Fusion* **47**, 1213 (2007).
- ⁵⁷T. Klinger, J. A. Alonso, S. A. Bozhnikov, R. Burhenn, A. Dinklage, G. Fuchert, J. Geiger, O. Grulke, A. Langenberg, M. Hirsch, G. Kocsis, J. Knauer, A. Krämer-Flecken, H. Laqua, S. A. Lazerson, M. Landreman, H. Maaßberg, S. Marsen, M. Otte, N. A. Pablant, E. Pasch, K. Rahbarnia, T. Stange, T. Szepesi, H. Thomsen, P. Traverso, J. L. Velasco, T. Wauters, G. Weir, T. Windisch, and the Wendelstein 7-X Team, "Performance and properties of the first plasmas of Wendelstein 7-X," *Plasma Phys. Controlled Fusion* **59**, 014018 (2017).
- ⁵⁸F. Jenko, W. Dorland, and G. W. Hammett, "Critical gradient formula for toroidal electron temperature gradient modes," *Phys. Plasmas* **8**, 4096–4104 (2001).
- ⁵⁹Y. Ren, S. M. Kaye, E. Mazzucato, W. Guttenfelder, R. E. Bell, C. W. Domier, B. P. LeBlanc, K. C. Lee, N. C. Luhmann, Jr., D. R. Smith, and H. Yuh, "Density gradient stabilization of electron temperature gradient driven turbulence in a spherical tokamak," *Phys. Rev. Lett.* **106**, 165005 (2011).
- ⁶⁰J. Ruiz Ruiz, Y. Ren, W. Guttenfelder, A. E. White, S. M. Kaye, B. P. Leblanc, E. Mazzucato, K. C. Lee, C. W. Domier, D. R. Smith, and H. Yuh, "Stabilization of electron-scale turbulence by electron density gradient in national spherical torus experiment," *Phys. Plasmas* **22**, 122501 (2015).
- ⁶¹G. Plunk, P. Xanthopoulos, G. Weir, S. A. Bozhnikov, A. Dinklage, G. Fuchert, J. Geiger, M. Hirsch, U. Hoefel, M. Jakubowski, A. Langenberg, N. A. Pablant, E. Pasch, T. Stange, D. Zhang, and the Wendelstein 7-X Team, "Stellarators resist turbulent transport on the electron larmor scale," *Phys. Rev. Lett.* **122**, 035002 (2019).
- ⁶²E. Gusakov and A. Surkov, "Spatial and wavenumber resolution of Doppler reflectometry," *Plasma Phys. Controlled Fusion* **46**, 1143 (2004).
- ⁶³E. Blanco and T. Estrada, "Study of Doppler reflectometry capability to determine the perpendicular velocity and the k-spectrum of the density fluctuations using a 2D full-wave code," *Plasma Phys. Controlled Fusion* **50**, 095011 (2008).
- ⁶⁴W. Horton, "Drift waves and transport," *Rev. Mod. Phys.* **71**, 735 (1999).
- ⁶⁵J. Riemann, R. Kleiber, and M. Borchardt, "Effects of radial electric fields on linear ITG instabilities in W7-X and LHD," *Plasma Phys. Controlled Fusion* **58**, 074001 (2016).
- ⁶⁶J. Proll, P. Xanthopoulos, and P. Helander, "Collisionless microinstabilities in stellarators. II. Numerical simulations," *Phys. Plasmas* **20**, 122506 (2013).